

1 **Strong Warming over the Antarctic Peninsula during Combined Atmospheric**  
2 **River and Foehn Events: Contribution of Shortwave Radiation and**  
3 **Turbulence**

4  
5 **Xun Zou<sup>1</sup>, Penny M. Rowe<sup>2</sup>, Irina Gorodetskaya<sup>3,4</sup>, David H. Bromwich<sup>5</sup>, Matthew A.**  
6 **Lazzara<sup>6</sup>, Raul R. Cordero<sup>7</sup>, Zhenhai Zhang<sup>1</sup>, Brian Kawzenuk<sup>1</sup>, Jason M. Cordeira<sup>1</sup>,**  
7 **Jonathan D. Wille<sup>8</sup>, F. Martin Ralph<sup>1</sup>, Le-Sheng Bai<sup>5</sup>**

8  
9 <sup>1</sup> CW3E, Scripps Institution of Oceanography, University of California San Diego, CA, USA

10 <sup>2</sup> NorthWest Research Associates, Redmond, WA, USA.

11 <sup>3</sup> CESAM - Centre for Environmental and Marine Studies, Department of Physics, University of  
12 Aveiro, Aveiro, Portugal.

13 <sup>4</sup> IIMAR | Interdisciplinary Centre of Marine and Environmental Research of the University of  
14 Porto, Porto, Portugal

15 <sup>5</sup> Byrd Polar and Climate Research Center, The Ohio State University, Columbus, OH, USA.

16 <sup>6</sup> Antarctic Meteorological Research and Data Center, Space Science and Engineering Center,  
17 University of Wisconsin-Madison, and Department of Physical Sciences, School of Engineering,  
18 Science, and Mathematics, Madison Area Technical College, Madison, WI, USA.

19 <sup>7</sup> Department of Physics, University of Santiago de Chile, Av. Bernardo O'Higgins 3363,  
20 Santiago, Chile.

21 <sup>8</sup> IGE/CNRS, University Grenoble-Alpes, France.

22  
23  
24 Corresponding authors: Xun Zou (x4zou@ucsd.edu) and Penny Rowe (penny@nwra.com)

25  
26  
27 **Key Points:**

- 28 • This study investigates the atmospheric river and foehn warming over the Antarctic  
29 Peninsula via observations and model simulations.  
30 • Under the combined atmospheric rivers and foehn, shortwave radiation contributed to the  
31 ice surface warming, followed by sensible heat flux.  
32 • Atmospheric rivers influence the foehn via extra moisture, which led to precipitation on  
33 the upwind side and cloud formation on the leeside.

34 **Abstract**

35 The Antarctica Peninsula (AP) has experienced more frequent and intense surface melting in  
36 recent years, jeopardizing the stability of ice shelves and ultimately leading to ice loss. Among  
37 the key phenomena that can initiate surface melting are atmospheric rivers (ARs) and leeside  
38 foehn; the combined impact of ARs and foehn led to moderate surface warming over the AP in  
39 December 2018 and record-breaking surface melting in February 2022. This study uses high-  
40 resolution Polar WRF simulations with advanced model configurations, Reference Elevation  
41 Model of Antarctica topography information, and surface observed albedo to improve our  
42 understanding of the relationship between ARs and foehn and their impacts on surface warming.  
43 With an intense AR (AR3) intrusion during the 2022 event, weak low-level blocking and heavy  
44 orographic precipitation on the upwind side resulted in latent heat release, which led to a more  
45 deep-foehn like case. On the leeside, sensible heat flux associated with the foehn magnitude was  
46 the major driver during the night and the secondary contributor during the day due to a stationary  
47 orographic gravity wave. Downward shortwave radiation was enhanced via cloud clearance,  
48 especially after the peak of the AR/foehn events, and dominated surface warming over the  
49 northeastern AP during the daytime. However, due to the complex terrain of the AP, ARs can  
50 complicate the foehn event by transporting extra moisture to the leeside via gap flows. During  
51 the peak of the 2022 foehn warming, cloud formation on the leeside hampered the downward  
52 shortwave radiation and slightly increased the downward longwave radiation.

53

54 **Plain Language Summary**

55 On the Antarctic Peninsula (AP), when ice shelves break up, glaciers flow faster from the land  
56 into the sea, leading to ice loss and increasing sea level rise. Surface warming may have led to  
57 ice shelf collapse and is projected to double by 2050 over Antarctica. Two phenomena that have  
58 enhanced surface warming are atmospheric rivers, (long corridors of moisture in the atmosphere)  
59 and leeside foehn effects (cooler and moist air advection on the upwind side and becomes  
60 warmer and drier when descending on the leeside). Here we study two combined atmospheric  
61 river and foehn events that led to surface warming on the AP, occurring in December 2018 and  
62 February 2022. The main warming mechanism in the northeastern AP during the nighttime was  
63 transfer of heat from the air to the ice surface (sensible heat flux), while the main mechanism  
64 during the daytime was intense sunlight, which was able to reach the surface because of clear  
65 skies on the opposite (lee) side caused by foehn. However, complicating the picture, there are  
66 gaps in the AP mountain range that let the atmospheric river through, allowing clouds to form on  
67 the other side, which then blocked some of the sunlight.

68

69 Key Words: Atmospheric River, Foehn Warming, Antarctic Peninsula, Polar AR Scale

## 70 1. Introduction

71 The Antarctica Peninsula (AP) is one of Earth's fastest warming regions and has been  
72 experiencing intense ice loss, especially since the early 2000s (Shepherd et al. 2018; Jones et  
73 al. 2019). Surface melting due to atmospheric warming is the major contributor to ice shelf  
74 break-up over the AP (e.g., van den Broeke 2005). In response to rapidly warming air  
75 temperatures, such as heat waves, surface melt is projected to increase in upcoming decades  
76 regardless of the emission scenario (Feron et al. 2021). Several Antarctic ice shelves have an  
77 increasing probability of reaching the record meltwater production that the Larsen A and  
78 Larsen B ice shelves exhibited before their collapse (Feron et al. 2021).

79 The rate of ice loss over the AP has tripled since the 1990s with an acceleration of  
80  $16 \text{ Gt yr}^{-1}$  per decade (Rignot et al. 2019; Shepherd et al. 2018). Also, surface melting is  
81 projected to double by 2050 over Antarctica, especially over the AP, which can decrease the  
82 surface albedo and lead to the ice surface lowering and thinning (Tuckett et al. 2019; Paolo et  
83 al. 2015; Siegert et al. 2019). Surface meltwater produced during the warming will not only  
84 jeopardize the stability of ice shelves via hydrofracturing, but also release latent heat if the  
85 melting water in the perennial snowpack refreezes, and then lead to additional melting  
86 (Holland et al. 2011). In the past three decades, the northern AP has lost the Larsen A Ice  
87 Shelf in 1995 and the Larsen B Ice Shelf in 2002 (Rignot et al. 2004; Rott et al. 1996).  
88 Without the buttressing effect provided by ice shelves, ice loss over Antarctica will  
89 accelerate and contribute to global sea level rise. From 2003 to 2019, the floating and  
90 grounded ice loss over the AP has contributed 1.7mm to sea level rise and has the potential to  
91 increase the sea level by 0.5m if all ice melts (Smith et al. 2020).

92           The collapse of ice shelves over the AP is the consequence of multiple factors,  
93 including rapid regional atmospheric warming and an extended melting period (Mulvaney et  
94 al. 2012; Scambos et al. 2000). During the austral summer, warming over the northeast AP is  
95 strongly associated with strengthening westerly winds due to the positive Southern Annular  
96 Mode (SAM) trend (Clem et al. 2016, 2022; Marshall et al. 2006; Elvidge and Renfrew  
97 2016). Stronger summer westerly winds (associated with a positive trend in the SAM) have  
98 led to a higher frequency of air masses being advected eastward over the orographic barrier  
99 of the northern Antarctic Peninsula (Marshall et al. 2006), contributing to foehn-induced  
100 surface melt of ice shelves on the Eastern side of the Peninsula (Bozkurt et al. 2018;  
101 González-Herrero et al. 2022). Also, deep convection in the central tropical Pacific often  
102 leads to prolonged cyclone activity over the South Pacific and blocking highs/anticyclones  
103 over the Drake Passage, which helps transport warm marine air towards the southwest AP  
104 (Clem et al. 2022). This circulation pattern may be associated with strong atmospheric rivers  
105 (ARs) and foehn warming on the leeside of the AP due to orographic lifting on the upwind  
106 side (Clem et al. 2022). However, the surface warming/melting pattern depends on the  
107 strength and landfall location of an AR, as well as its modification by the local topography.

108           Previous ice shelf break-ups have been influenced by ARs and foehn (Wille et al.  
109 2022). Polar ARs are moisture from lower latitudes that travel to the polar region via a long  
110 narrow corridor of water vapor transport (Ralph et al. 2004; Wille et al. 2022; Gorodetskaya  
111 et al. 2020; Terpstra et al. 2021). Foehn wind is a warm and dry descending air on the leeside  
112 of the mountain barrier, which results from relatively cooler and moist air advection on the  
113 upwind side (WMO, 1992). ARs can trigger foehn warming and lead to record-breaking  
114 temperatures, such as the warm event (max 2m temperature of 17.5°C) observed at

115 Esperanza station in March 2015 (Bozkurt et al. 2018; Xu et al. 2021). Foehn warming in the  
116 polar regions triggered by ARs has been observed over the AP (e.g., Bozkurt et al. 2018;  
117 Wille et al. 2019), West Antarctica (eastern Ross Ice Shelf, Zou et al. 2021a), and Greenland  
118 (Mattingly et al. 2020). Standalone foehn events (without AR impacts) may generally have a  
119 smaller warming extent across the Larsen ice shelves than those associated with intense ARs  
120 (Wille et al. 2022)

121 A variety of mechanisms contribute to foehn warming, including latent heat release  
122 on the upwind side from orographic precipitation, adiabatic warming from the descending  
123 air, sensible heat transfer from upper foehn flow to the ice surface via turbulence, local  
124 topography, and enhanced radiative heating due to foehn clearance; in turn, these contribute  
125 to surface warming/melting on the leeside (Elvidge and Renfrew 2016). Larsen Ice Shelf is  
126 frequently under the impact of foehn warming, especially at the mountain base and the  
127 northern AP region (Turton et al. 2018). Extra moisture flux from ARs can amplify foehn  
128 warming due to increased latent heat release (Bozkurt et al. 2018). Thus, analysis of detailed  
129 mechanisms of surface warming under combined ARs and foehn can help us better  
130 understand the ice shelf stability and will benefit future projections of sea level rise.

131 Despite knowledge gains from previous studies, the detailed physical mechanism of  
132 surface melting on the AP under the combined impact of ARs and foehn is still unclear. First,  
133 with different circulation patterns, the water vapor flux or transport within the AR may or  
134 may not hit the mountain range over the AP perpendicularly, which significantly affects the  
135 formation of the foehn wind. Also, the northern tip of the AP tilts eastward, which indicates  
136 that the southern and northern AP might experience different magnitudes of warming under  
137 the same foehn event. Second, the strength of radiative heating depends both on cloudiness

138 and on solar elevations, which are low over the AP. Previous studies have found radiative  
139 heating on the AP is relatively small in a deep-foehn case during early summer (Elvidge and  
140 Renfrew 2016); however, it is important to address whether this is always the case. Third, the  
141 topographic barrier over the AP has several gaps (or lower elevations), which can allow extra  
142 moisture from ARs to reach the leeside directly (e.g., foehn jets; Laffin et al. 2022). This can  
143 weaken the intensity of orographic precipitation on the upwind side and foster cloud  
144 formation from the extra moisture on the leeside, complicating the foehn-cloud clearance  
145 effect (Elvidge et al. 2020) by reducing the shortwave downward radiation (SWD), and thus  
146 the radiative heating. In addition, these foehn jets have contributed to surface melting due to  
147 enhanced sensible heat flux (SHF) transfer (Elvidge et al. 2015).

148 This work investigates two representative AR/foehn cases in 2018 and 2022 via high-  
149 resolution Polar Weather Research and Forecasting model (PWRF) simulations with  
150 advanced model configurations. Section 2 describes the data and PWRF model settings.  
151 Section 3 presents the evaluation of PWRF simulations by comparison to observations from  
152 weather stations and radiosondes, analyzes the regional circulation pattern, and investigates  
153 the contribution of AR/foehn to the leeside warming. Section 4 discusses the relationship  
154 between AR and foehn in the 2022 case, and their combined impact on the surface melting. A  
155 comparison of AR/foehn cases between the AP and West Antarctica (WA) is also presented.  
156 Section 5 summarizes the results from the previous analysis.

157

## 158 2. Data and Methods

### 159 2.1. ERA5 reanalysis data

160 This study uses the 5<sup>th</sup> major atmospheric reanalysis (ERA5) and the land dataset  
161 (ERA5 Land) produced by the European Centre for Medium-Range Weather Forecasts  
162 (ECMWF). By combining model simulations with observations, ERA5 provides hourly  
163 output with 31km horizontal resolution and 137 vertical levels. Compared to its predecessor,  
164 ERA-Interim, ERA5 significantly improved results in the troposphere with a shorter latency,  
165 including conservation of potential temperature (Hersbach et al. 2020; Hoffmann et al. 2019).  
166 Synoptic- and meso-scale features, such as cyclones, convective updrafts and gravity waves  
167 are better described in ERA5 (Hoffmann et al. 2019). Also, ERA5 outperforms other  
168 reanalysis products in describing stratospheric ozone depletion, which is critical for  
169 atmospheric changes in the high-latitude Southern hemisphere (Davis et al. 2017; Hersbach  
170 et al. 2020). Over the AP, ERA5 provides reliable information on surface temperature, wind  
171 speed, and humidity, especially at higher elevations (Tetzner et al. 2019). ERA5 Land with 9  
172 km horizontal resolution is used to provide surface melting conditions for the case study.  
173 Driven by ERA5, ERA5 Land implements a correction in the thermodynamic near-surface  
174 state and reduces the error in skin temperature (Muñoz-Sabater et al. 2021).

175

## 176 2.2. Observations

177 PWRP surface simulations, including surface pressure, 2m temperature, and 10m  
178 wind speed were compared to station observations (Escudero; upwind side) and observations  
179 from Automatic Weather Stations (AWS) or manual stations on the upwind side (Vernadsky  
180 and Rothera) and on the lee side (Esperanza, Marambio, and Larsen C). Weather station data  
181 were obtained from the Antarctic Meteorological Research and Data Center (AMRDC;  
182 <https://amrdcdata.ssec.wisc.edu/>) at the University of Wisconsin-Madison (Lazzara et al.

183 2012), and from the QGIMET website (<https://www.ogimet.com/>). Three-hourly  
184 observations were used.

185 In addition, this study uses Antarctic composite infrared satellite imagery data for  
186 both 2018 and 2022 cases from the AMRDC at the University of Wisconsin-Madison. The  
187 Worldview tool from NASA's Earth Observing System Data and Information System  
188 (EOSDIS) provides additional satellite imagery on cloud conditions over the AP. Daily cloud  
189 conditions are observed from Moderate Resolution Imaging Spectroradiometer (MODIS)  
190 Corrected Reflectance (utilized from MODIS Level 1B data) on the Aqua and Terra  
191 satellites.

192 PWRP atmospheric profiles of temperature, humidity, and winds are compared to all  
193 available radiosonde measurements from three Antarctic stations: Escudero, Rothera and  
194 Marambio for the two case study periods (see columns 1-3 of Table 3 for 2022 and Table S1  
195 for 2018). At Rothera, radiosondes were launched almost daily at 12UTC during 2018-2022.  
196 Unfortunately, only one radiosonde was launched at Rothera during the 2022 case study. At  
197 Marambio, radiosondes were launched less frequently, and only one radiosonde is available  
198 for each case study. By contrast, intensive extra observing activities were conducted at  
199 Escudero during the two case study time periods (including launching 7 radiosondes in 2018  
200 and 5 radiosondes in 2022) as part of the Polar Prediction Project (PPP), a 10-yr (2013–22)  
201 initiative of the World Meteorological Organization's (WMO) World Weather Research  
202 Programme (WWRP) (Bromwich et al. 2020; Gorodetskaya et al., 2022).

203 The AP ice shelves experience persistent summer melt ponds, and surface melting  
204 and refreezing reduce the surface albedo, leading to a positive snowmelt-albedo feedback and  
205 accelerating melting (Jakobs et al. 2021; Feron et al. 2021). Thus an accurate model surface

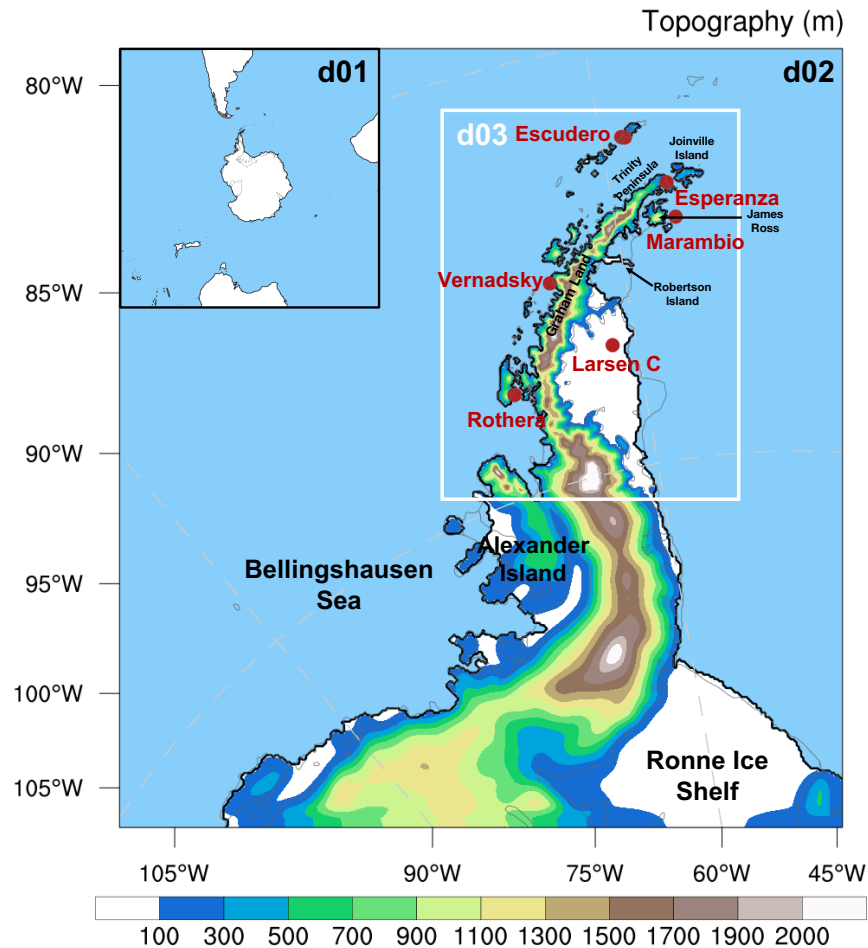
206 description in PWRF is critical for the estimation of surface warming/melting (Luckman et  
207 al. 2014; Turton et al. 2018). Instead of the arbitrary default albedo in WRF, we use observed  
208 daily surface albedo from MODIS as an initial field in model simulations (hereafter referred  
209 to as MODIS albedo; Wang et al. 2015; Figs. S1a and b). The MODIS albedo is produced by  
210 the National Aeronautics and Space Administration (NASA) based on 16 days of Terra and  
211 Aqua MODIS observational data. The MODIS albedo has been tested in the surface melting  
212 study over West Antarctica, where it was shown to lead improvements in the surface  
213 temperature estimation (Zou et al. 2021a). Also, the systematic cold bias over the Tibetan  
214 Plateau in WRF has been reduced by including the MODIS albedo. Created from  
215 stereophotogrammetry and satellite imagery, the Reference Elevation Model of Antarctica  
216 (REMA) provides a high-resolution surface elevation dataset with a spatial resolution of up  
217 to 8m (Howat et al. 2019; Gerber and Lehning 2020). REMA surface elevation at 1km  
218 resolution is introduced in PWRF simulations to better describe the modifications of the  
219 airflows by the local topography.

220

### 221 2.3. Polar WRF and Antarctic Mesoscale Prediction System (AMPS)

222 Developed and maintained by the Polar Meteorology Group of the Byrd Polar and  
223 Climate Research Center at The Ohio State University (Hines and Bromwich 2008;  
224 Bromwich et al. 2013; Listowski and Lachlan-Cope 2017; Hines et al. 2019), PWRF is a  
225 regional numerical prediction model based on WRF. This study used PWRF V4.3.3 to  
226 produce hourly output with a downscaling method, which includes 30-km-resolution domain  
227 1, 6-km resolution domain 2, and a 1.2 km high-resolution domain 3 covering the AP region

228 (Fig. 1). All PWRF outputs used in this paper are initialized at 00UTC, discarding the first  
 229 24h as spin-up time.



230

231 **Figure 1.** PWRF domain with Reference Elevation Model of Antarctica (REMA)  
 232 topography. Red dots indicate locations of available surface stations.  
 233

234

Table 1 shows the input data and physical parameterization settings in PWRF.

235

Supercooled water in clouds is always challenging to predict in the numerical weather  
 236 models over the Southern Ocean (e.g., Bodas-Salcedo et al. 2016; Listowski et al. 2019).

237

More advanced microphysics schemes provide more realistic cloud liquid water simulations,  
 238 which is critical for estimation of the surface energy balance (Hines et al. 2019; Listowski et

239

al. 2019). Instead of using an arbitrary categorization of frozen hydrometers, the two-moment

240 Morrison–Milbrandt P3 (P3) adopts a continuum of particle properties for clouds (Hines et al.  
 241 2019, 2021). P3 provides the best estimation of liquid water path and longwave radiation  
 242 from clouds compared to two other advanced schemes, Morrison two moment and Thompson  
 243 (Hines et al. 2019). Thus, P3 is selected for the microphysics scheme, and the Mellor–  
 244 Yamada–Nakanishi–Niino (MYNN; Nakanishi and Niino 2006) is used for the atmospheric  
 245 boundary layer scheme. Both longwave and shortwave radiation use the Rapid Radiative  
 246 Transfer Model (RRTMG; Clough et al. 2005) or Global Climate/Circulation Models. We  
 247 also use the Kain–Fritsch scheme for cumulus parameterization and Noah-MP for the land  
 248 surface model (Kain 2004; Niu et al. 2011). Most importantly, REMA 1km topography  
 249 information and MODIS surface observed albedo, described previously, are included in the  
 250 input data to provide a better surface description (Howat et al. 2019; Corbea-Pérez et al.  
 251 2021; Fig. S1). To avoid model instabilities, topographic smoothing has been applied to  
 252 PWRf simulations. Adopting several PWRf settings, the Antarctic Mesoscale Prediction  
 253 System (AMPS) outputs are used in this paper to provide default albedo and landmass in  
 254 PWRf. AMPS, developed by the National Center for Atmospheric Research (NCAR),  
 255 provides high-resolution weather forecasts to support the operations of the US Antarctic  
 256 Program (Powers et al. 2012).

257 **Table 1.** PWRf model setting.

|                        | <b>PWRf V4.3.3</b>                            |
|------------------------|---|
| Input data             | ECMWF reanalysis data (ERA5)                  |
| Horizontal resolution  | 30 km / 6 km / 1.2km                          |
| Vertical levels        | 71 levels (lowest level 4m above the surface) |
| Temporal resolution    | hourly  |
| Spin-up                | 24h   |
| Microphysics           | P3  |
| PBL scheme             | MYNN  |
| Shortwave and longwave | Both RRTMG                                    |

|                            |   |
|----------------------------|---|
| Land surface options       | Noah MP   |
| Surface layer options      | MYNN  |
| Surface albedo             | MODIS (MODIS/Terra+Aqua BRDF/Albedo Albedo Daily L3 Global 0.05 Deg; black-sky albedo)                                |
| High-resolution topography | REMA 1km topography   |
| Nudging                    | Every 6 hours; nudging to u, v wind, temperature, and water vapor from ERA5 for model level 40 (~ 400 hPa) and above. |

258

259 

## 2.4. Polar Atmospheric River Scale

260 Compared to the mid- and low-latitudes, Antarctica has a colder, drier, and more  
 261 pristine environment. Thus, the Center for Western Weather and Water Extremes (CW3E)  
 262 group developed an AR scale specific to the polar regions, the Polar AR scale (7 rankings  
 263 from AR A1 to AR5; Fig. S2), to rank ARs over the AP at a given geographic location (Fig.  
 264 S2). The Polar AR scale was widely tested during the Year of Polar Prediction in the  
 265 Southern Hemisphere (YOPP-SH) Winter Targeted Observing Periods, and has been proven  
 266 to reflect the strength and duration of ARs accurately, which benefits both forecast operations  
 267 and research (Bromwich et al. 2020; Ralph et al. 2019; Zhenhai et al., 2023).

268 After using PWRF domain 3 outputs to identify AR intrusions, the hourly integrated  
 269 vapor transport (IVT) is calculated as follows:

$$270 \quad IVT = \sqrt{\left(\frac{1}{g} \int_{1000}^{10} qu dp\right)^2 + \left(\frac{1}{g} \int_{1000}^{10} qv dp\right)^2} \quad (1),$$

271 where  $g$  is the gravity acceleration constant ( $m s^{-2}$ ),  $q$  is specific humidity ( $kg kg^{-1}$ ),  $u$  and  $v$   
 272 are zonal and meridional wind ( $m s^{-1}$ ), and  $dp$  is the differential pressure (hPa).

273

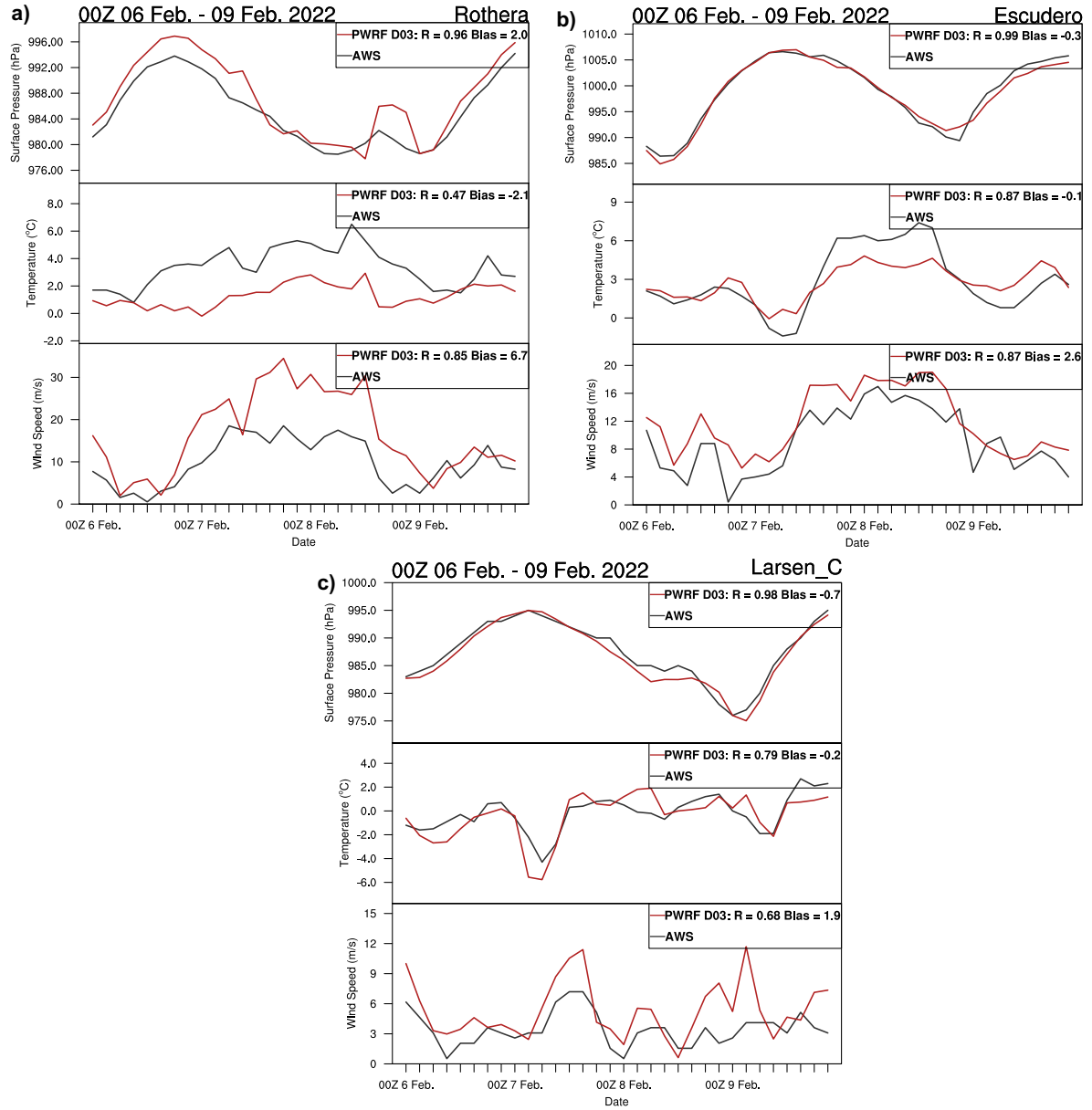
274 

## 3. Results

275 

### 3.1. Evaluation of PWRF results

276 PWRF simulation outputs were compared to station and AWS 3-hourly observations  
277 and ERA5 reanalysis data. Overall, PWRF was found to reliably simulate the synoptic  
278 circulation pattern (not shown) and surface conditions compared to ERA5. Figure 2 shows  
279 the comparison of 3 basic surface variables between weather station observations and PWRF  
280 domain 3 outputs at Rothera (upwind) and Larsen C (leeside) during the 2022 case. PWRF  
281 simulations have a weak negative bias ( $-0.2\text{ }^{\circ}\text{C}$ ) in temperature and a moderate positive bias  
282 in wind speed ( $1.9\text{ m/s}$ ) at the Larsen C Ice shelf. At Rothera, where the topography is  
283 complex, PWRF has a larger bias in all variables, especially for the 10m wind speed during  
284 the peak of the foehn warming. The  $1.2\text{ km}$  horizontal resolution might be insufficient to  
285 capture the complex terrain on the upwind side. Thus, PWRF performs better in general at  
286 stations with a smoother surface. In addition, the average bias of 2m relative humidity is 5%  
287 at Marambio and 1.3% at Escudero. On average, PWRF biases (Table 2) were found to be  
288  $0.82\text{ hPa}$  in surface pressure,  $-1.22\text{ }^{\circ}\text{C}$  in 2m temperature, and a  $4.38\text{ m/s}$  in 10 m wind speed  
289 ( $2.6\text{ m/s}$  on the leeside and  $6.2\text{ m/s}$  on the upwind side) at the selected AWS stations. In  
290 addition, compared with ERA5, PWRF simulations show a stronger barrier jet on the upwind  
291 side; further investigation into this result is needed.



292

293

294

295

**Figure 2.** Evaluation of PWRP simulations based on observations at Rothera, Escudero, and Larsen C weather stations every 3 hours.

296

297

**Table 2.** PWRP correlation coefficient (R) and bias at several weather stations based 3hrly data from 0000UTC 6 February to 2100UTC 9 February 2022.

| Stations  | Surface pressure (hPa) |      | Temperature (°C) |      | Wind speed (m/s) |      |
|-----------|------------------------|------|------------------|------|------------------|------|
|           | R                      | Bias | R                | Bias | R                | Bias |
| Rothera   | 0.96                   | 2.0  | 0.47             | -2.1 | 0.85             | 6.7  |
| Vernadsky | 0.96                   | -0.3 | 0.78             | 0    | 0.54             | 9.2  |
| Escudero  | 0.99                   | -0.3 | 0.87             | -0.1 | 0.87             | 2.6  |

|                |             |             |             |              |             |             |
|----------------|-------------|-------------|-------------|--------------|-------------|-------------|
| Marambio       | 0.99        | 2.2         | 0.53        | -3.3         | 0.74        | 1.2         |
| Larsen C       | 0.96        | -0.7        | 0.79        | -0.2         | 0.68        | 1.9         |
| Esperanza      | 0.94        | 2.0         | 0.27        | -1.6         | 0.25        | 4.7         |
| <b>Average</b> | <b>0.97</b> | <b>0.82</b> | <b>0.62</b> | <b>-1.22</b> | <b>0.66</b> | <b>4.38</b> |

\*Gray shadow indicates stations located on the upwind side.

298  
299

300 PWRF temperatures, relative humidities, and wind speeds in the troposphere were  
301 compared to station radiosonde measurements (Figs. S3a and S3b). Absolute maximum,  
302 mean, and root mean square differences for temperature and wind speed are summarized in  
303 Table 3 for 2022 (and in Table S2 for 2018). In 2022, the root-mean-square (RMS)  
304 difference in tropospheric temperature was 1.1 °C (absolute maximum of 3.3 °C and mean  
305 bias of -0.2 °C), and the RMS difference in tropospheric wind speed was 3.7 m/s (absolute  
306 maximum of 10 m/s and mean bias of 0.9 m/s). Differences in 2018 (Table S1) were similar.  
307 Differences for relative humidity (RH) are complicated by high variability and occasional  
308 low biases in the radiosonde RH measurements they are given in tables S2 and S3. The  
309 overall good performance discussed above provides high confidence for us to use the PWRF  
310 simulation to analyze the two surface warming events over the AP.

311 **Table 3.** PWRF maximum (max; absolute) differences, mean biases (Mean) and root mean  
312 square differences (RMS) in tropospheric temperature and wind speed, relative humidity  
313 (RH) and wind speed at several stations during the 2022 case study.

| Stations       | Date     | Time | Temperature (°C) |             |            | Wind speed (m/s) |            |            |
|----------------|----------|------|------------------|-------------|------------|------------------|------------|------------|
|                |          |      | Max              | Mean        | RMS        | Max              | Mean       | RMS        |
| Escudero       | 2022/2/7 | 0    | 2.6              | -0.1        | 0.7        | 6.7              | 0.9        | 2.0        |
|                | 2022/2/7 | 12   | 2.1              | -0.1        | 0.6        | 9.5              | 0.6        | 4.3        |
|                | 2022/2/8 | 0    | 3.5              | -0.3        | 1.2        | 20.0             | 2.5        | 5.1        |
|                | 2022/2/8 | 23   | 4.2              | 0.2         | 1.5        | 7.4              | -0.9       | 2.9        |
|                | 2022/2/9 | 12   | 2.0              | -0.2        | 0.9        | 8.0              | 0.8        | 3.3        |
| Rothera        | 2022/2/9 | 12   | 5.8              | -0.2        | 1.6        | 8.4              | 1.3        | 4.5        |
| Marambio       | 2022/2/7 | 12   | 2.9              | -0.8        | 1.3        | 10.8             | 0.8        | 3.5        |
| <b>Average</b> |          |      | <b>3.3</b>       | <b>-0.2</b> | <b>1.1</b> | <b>10.1</b>      | <b>0.9</b> | <b>3.7</b> |

314 \*Gray shadow indicates stations located on the upwind side. The absolute bias, mean bias,  
315 and RMS are the average values of 27 pressure levels, from 100hPa to 1000hPa by 25hPa.  
316

### 317 3.2. December 2018 and February 2022 surface melt events over the Antarctic Peninsula

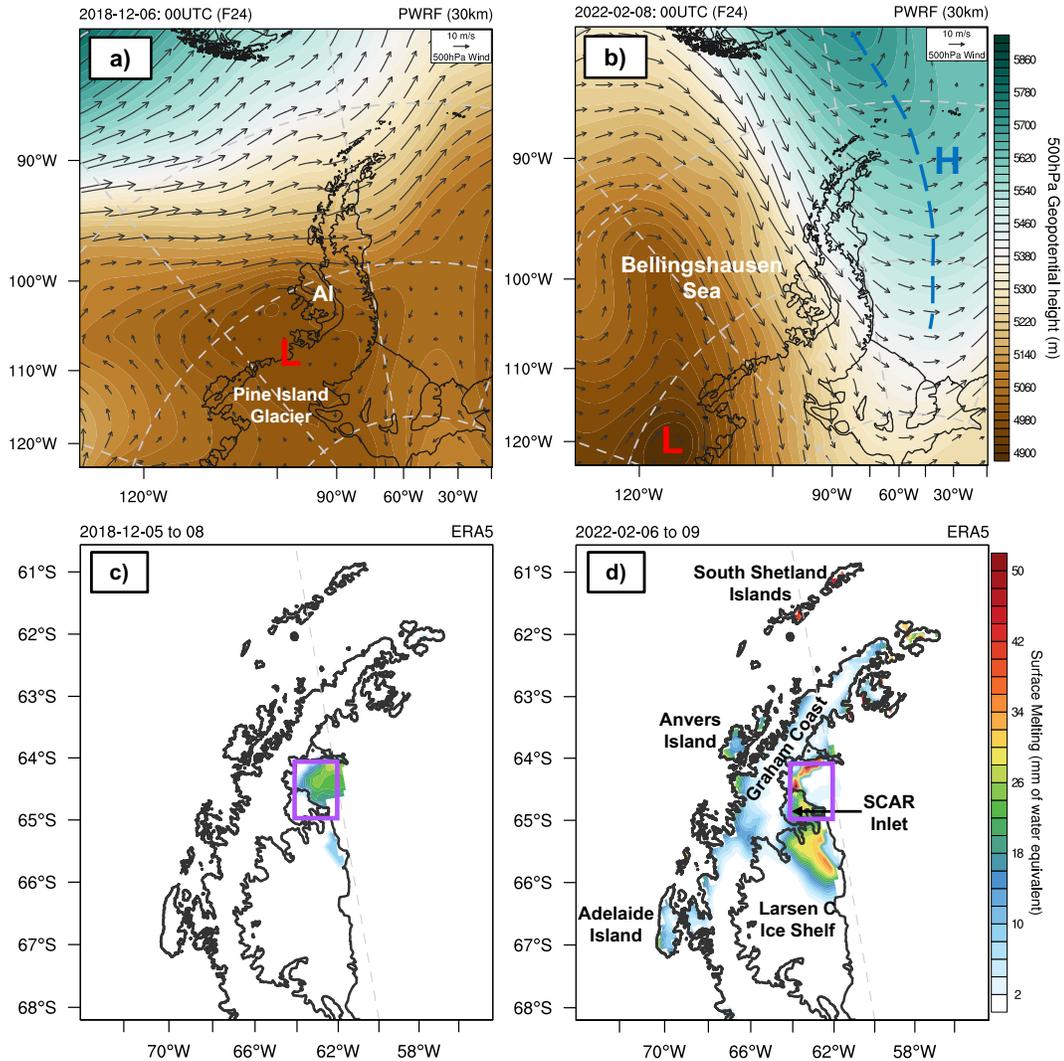
318 Two surface melting events that were triggered by the combined impact of ARs and  
319 foehn warming are studied, occurring on the northern AP in December 2018 and February  
320 2022. In December 2018, a high precipitation amount (up to 5.7mm/day) was observed at  
321 Vernadsky (Chyhareva et al. 2021), and surface melting also detected on the leeside based on  
322 National Snow and Ice Data Center (NSIDC) daily surface melt extent (not shown). At the  
323 beginning of January 2022, a large expanse of sea ice (about 2,000 km<sup>2</sup>), which had persisted  
324 in the Larsen B embayment since 2011 and that can bond and stabilize the ice shelves, began  
325 to break up between 17 and 19 January 2022 (NASA, 2022). In the following February,  
326 under the La Niña condition and positive SAM (SAM index 1.92; Marshall 2003), an  
327 unprecedented warming caused major surface melt over both western and eastern AP  
328 (Gorodetskaya et al, 2022). On 7-8 February 2022, several Antarctic stations observed record  
329 high temperatures, such as +12.7 °C at Vernadsky, +13,6°C at Carlini, and +13.7 °C at King  
330 Sejong (Gorodetskaya et al, 2022). The air temperature at Escudero remained above +6 °C  
331 from 18UTC 7 February until 15UTC on 8 February.

332

### 333 3.3. Regional circulation and Atmospheric River

334 The regional circulation significantly affects the strength and direction of ARs, and  
335 local topography impacts the orographic precipitation. Figure 3 shows 500hPa geopotential  
336 height, horizontal wind from PWRP and the surface melting map from ERA5 Land for both  
337 2018 and 2022 cases (e.g., 00UTC 6 December and 00UTC 8 February). Although both cases  
338 featured the development and propagation of two low-pressure centers, location of the lows  
339 varied, as well as the circulation pattern. In the 2018 case, the first low-pressure center

340 developed over Pine Island Glacier at ~00UTC on 6 December (Fig. 3a), and the secondary  
341 low developed over the Weddell Sea at ~03UTC on 7 December (not shown). These two  
342 lows covered the entire AP region, which led to zonal marine air advection over the northern  
343 tip of the AP for ~24 hours. In the 2022 case, the first low was located at coastal Pine Island  
344 Glacier (Fig. 3b) and the second low migrated from the Bellingshausen Sea towards  
345 Alexander Island (not shown). Unlike the 2018 case, the 2022 case had a blocking high over  
346 the Weddell Sea (blue dashed line, Fig. 3b). This low-high coupled pattern not only led to a  
347 stronger pressure gradient and marine air intrusion but also resulted in a stationary northerly  
348 flow lasting for 3 days, which transported extra moisture and heat from lower latitudes to  
349 Antarctica (e.g., Hirasawa et al. 2013). Using two polar-specific AR detection algorithms  
350 (see Wille et al. 2021; Zhang et al. 2023), an AR was briefly detected northwest of the AP for  
351 the 2018 case, while in 2022, a prolonged AR was detected over the AP from 7-9 February  
352 following a shorter AR landfall on 5 February.



353  
 354 **Figure 3.** Circulation pattern and surface melting for the 2018 and 2022 cases. a) and b)  
 355 500hPa geopotential height (contours) and wind field (black arrows) from PWRF d01 (30km)  
 356 at 0000UTC 06 December 2018 and 08 February 2022. Blue “H” and dashed blue line  
 357 represent the blocking high, and red “L” represents the low-pressure center. c) and d) show  
 358 the 3-day accumulated surface melting of water equivalent based on hourly ERA5 Land  
 359 (9km) reanalysis data. AI: Alexander Island. The purple box in d) represents the AR/foehn  
 360 “hotspot”.  
 361

362 Compared to the 2018 case, the melting in the 2022 case impacts a broader area. In  
 363 the 2018 case, the surface melting was mainly over the remaining Larsen B Ice Shelf (max  
 364 ~30 mm of water equivalent; see Fig. 3c). By contrast, in the 2022 case, surface melting  
 365 affected the whole northern AP (Fig. 3d), including the upwind side (e.g., Anvers Island,

366 Graham Coast, and Adelaide Island; see also Gorodetskaya et al., 2022). The South Shetland  
367 Islands also experienced strong melting, whereas no melting was detected there in the 2018  
368 case. On the leeward side of the AP in the 2022 case, the intense melting (max >50 mm of water  
369 equivalent) covered the remaining Larsen B embayment, SCAR inlet, and the northern edge  
370 of the Larsen C Ice shelf, which are the focus areas of this research. The warming event in  
371 early February 2022 may have also contributed to the significant negative anomalies in sea  
372 ice extent observed in austral summer 2021-22. In late February 2022, sea-ice extent hit its  
373 annual minimum at 1.9 million km<sup>2</sup>, the absolute record low Antarctic sea-ice extent since  
374 the beginning of continuous satellite monitoring in 1979 (Wang et al. 2022a). Sea-ice extent  
375 remained close to record low levels during most of the summer 2021-22.

376           Using PWRP simulations, the maximum AR scale was found to be a moderate AR2  
377 (Fig. 4a), according to the Polar AR scale (Fig. S2). Consistent with the regional circulation,  
378 in 2018 the AR only affected the northern tip of the AP, as indicated by the IVT (Fig. 4c).  
379 During the 2022 event, the entire AP region, coastal Pine Island Glacier, and the Filchner–  
380 Ronne Ice Shelf were all under the strong impact of AR3 with a max AR4 over Adelaide  
381 Island (Figs. 4b and d; Table 4).

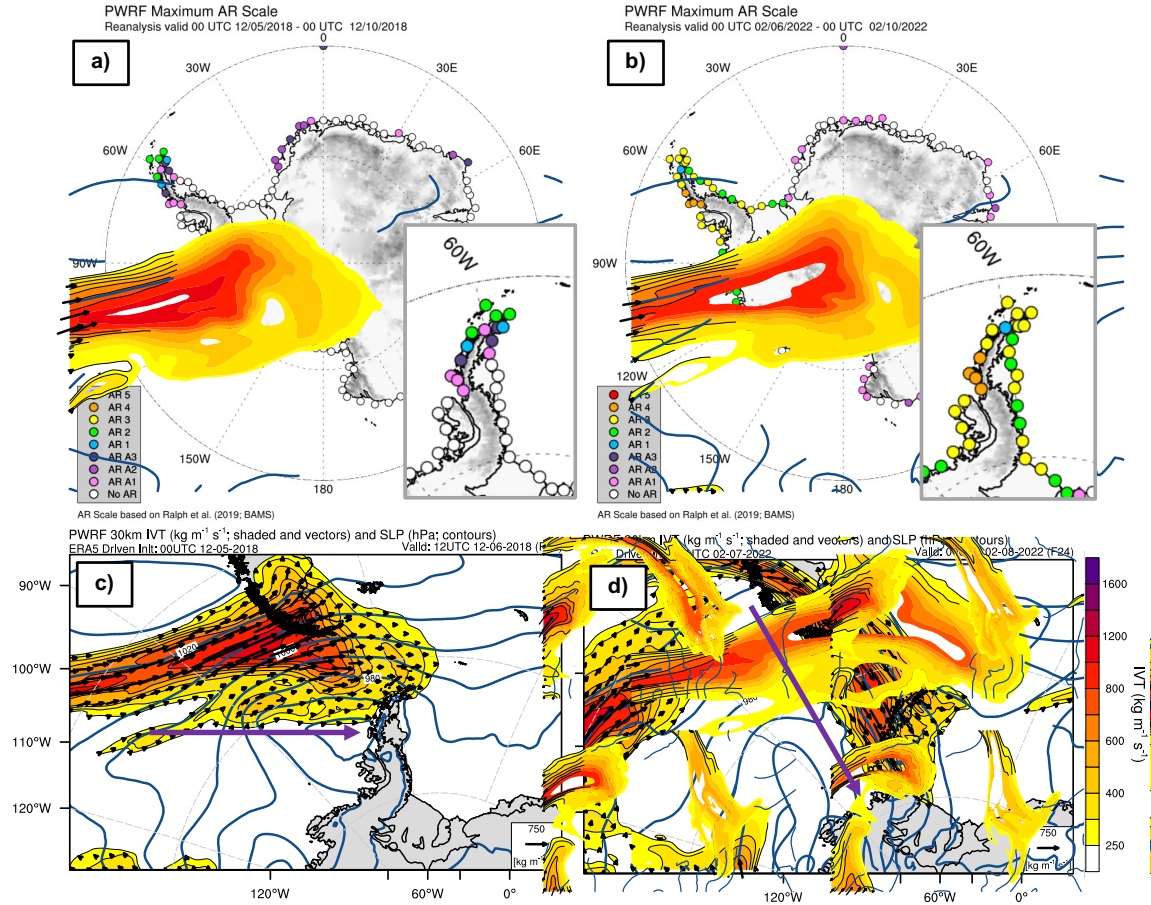


**Figure 4.** The Atmospheric River (AR) cases in 2018 and 2022 over the Antarctic Peninsula (AP). a), b) The adaption of CW3E Polar AR Scale for both cases. c), d) Integrated vapor transport (IVT) from PWRF d01 for both cases. Navy lines represent the mean sea level pressure (interval: 10 hPa).

382  
383  
384  
385  
386  
387  
388

**Table 4.** Overview of 2018 and 2022 cases.

|                     | 2018                                      | 2022   |
|---------------------|---|--|
| Maximum AR detected | AR2 (ERA5)                                | AR3 (ERA5) and AR4 (PWRF)  |
| AR duration         | 1 day                                     | 3 days   |
| AR impact area      | Upwind side of the northern tip of the AP | Entire AP region, coastal Pine Island Glacier and Ronne Ice Shelf. |
| AR direction        | AR hits the AP via southwesterly wind     | AR hits the AP via northwesterly wind                              |
| AR peak             | 2018-12-06 ~06UTC                         | 2022-02-07 ~00UTC @Palmer land region                              |

|                             |                   |  |
|-----------------------------|-------------------|--|
|                             |                   | 2022-02-07 ~12UTC @upwind side of the AP |
| Foehn peak                  | 2018-12-06 ~12UTC | 00UTC 02-08-2022 – 00UTC 02-09 2022      |
| Max. temp on the leese side | 11 °C             | 18 °C                                    |

389

390

391

392

393

394

395

396

397

398

399

400

401

402

403

404

405

406

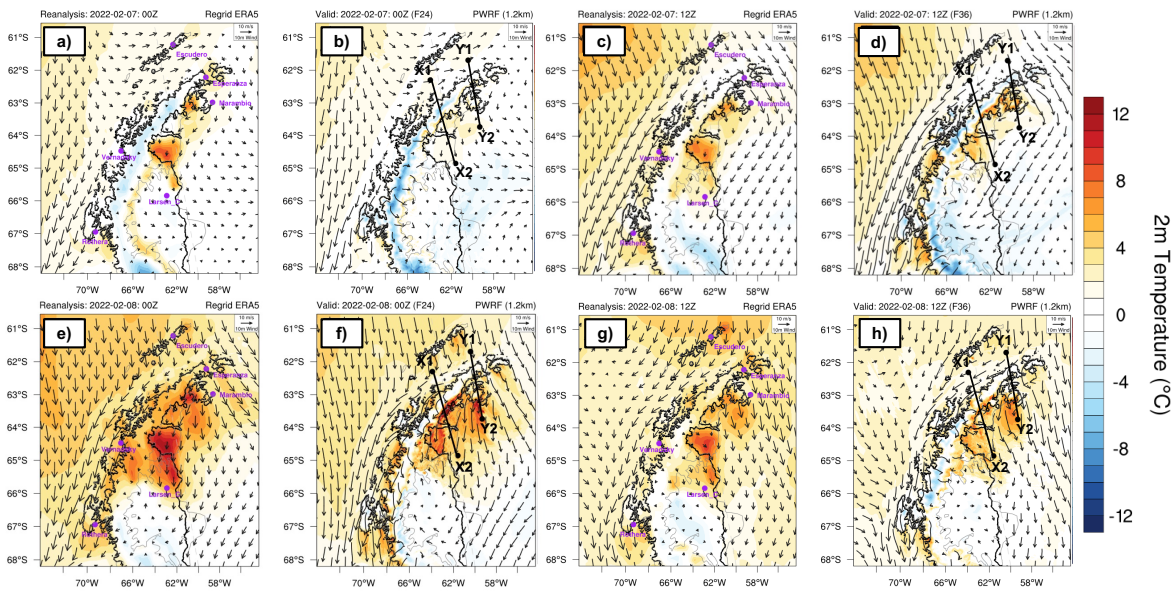
407

ERA5 generally agrees with PWRP on the AR scale, except for a few spots adjacent to Adelaide Island where ERA5 indicates AR3 (not shown). The IVT pattern clearly shows the difference between these two cases. With a more zonal wind during the 2018 event (Fig. S4a grey arrow, e.g., 06UTC 6 December 2018), southern Graham Land experienced nearly perpendicular moist air advection (Fig. S4a solid brown box). Under this circumstance, the Larsen C Ice Shelf was most likely under foehn warming. Over Trinity Peninsula, where the topographic barrier tilts eastward, the marine air intrusion approached the coast at a  $\sim 45^\circ$  angle (Fig. S4a blue dashed box). Thus, the foehn warming was weaker over the original Larsen A and B Ice Shelves (hereafter referred to as Larsen A and Larsen B). However, in the 2018 case, upcoming wind is not strong enough to trigger widespread foehn warming over the Larsen C Ice shelf, and Larsen A and B experienced moderate surface warming. By contrast, the 2022 case had a perpendicular airflow over the Trinity Peninsula due to a northerly wind pattern (Fig. S4b, grey arrow, e.g., 00UTC 8 February 2022), and the northern AP was under a stronger foehn warming (Fig. S4b solid blue box). The direction, strength, and duration of the noted ARs are important because they affect the magnitude of the foehn warming on the leese side.

### 3.4. Foehn warming and AR impacts

408 Both the 2018 and 2022 case experience foehn warming on the leeside, however this  
409 study focuses on the 2022 event due to its broader impact (Figs. 3c, 3d and 4). For the 2018  
410 case, the surface warming mainly occurs along the mountain base and then expands to the  
411 Larsen ice shelves, which only last for ~24 hours. Over the Larsen B region (indicated  
412 previously with a purple box in Fig. 3d), the average 2m temperature increased ~3°C within  
413 12 hours (from 00UTC 6 to 12UTC 6 December 2018) and above freezing point 2m  
414 temperature lasted for ~10 hours (Fig. S5a). The skin temperature (over land only) confirms a  
415 moderate surface melting that lasted ~6 hours during the foehn period. On the leeside of the  
416 AP, there are two warming spots during the 2022 foehn case. One is over the Larsen B  
417 embayment (including the SCAR Inlet) and the other is adjacent to James Ross Island (Fig.  
418 5). The Larsen C Ice shelf did not experience widespread warming, except for the northern  
419 edge. Over the Larsen B region (purple box in Fig. 3d), the average 2m temperature  
420 increased more than 5°C and the average 10m wind speed increased ~8m s<sup>-1</sup> within 24 hours  
421 (from 00UTC 7 to 00UTC 8 February 2022, second foehn period; Fig. S5b). The average 2m  
422 relative humidity dropped by 20% after the peak of AR/foehn impact (Fig. S5b). The above  
423 freezing point 2m temperature lasted for ~30 hours during the second foehn period, which  
424 was 3 times longer to the 2018 case. The skin temperature over ice shelves reached 0°C for  
425 29 hours and remained high even after the foehn warming. The barrier jets on the upwind  
426 side indicate weak low-level blocking (e.g., Figs. 5f and 5h). While both ERA5 and PWRP  
427 captured the two warming hotspots (Fig. 5), the 2m temperature in ERA5 was sometimes  
428 4 °C warmer than PWRP over Larsen B, especially at the beginning of this warming event  
429 (e.g., compare panels a and b in Fig. 5). Larsen B is a mixture of open water and floating ice  
430 during the 2022 case. ERA5 indicates this area as land/ice shelves based on its land-sea mask

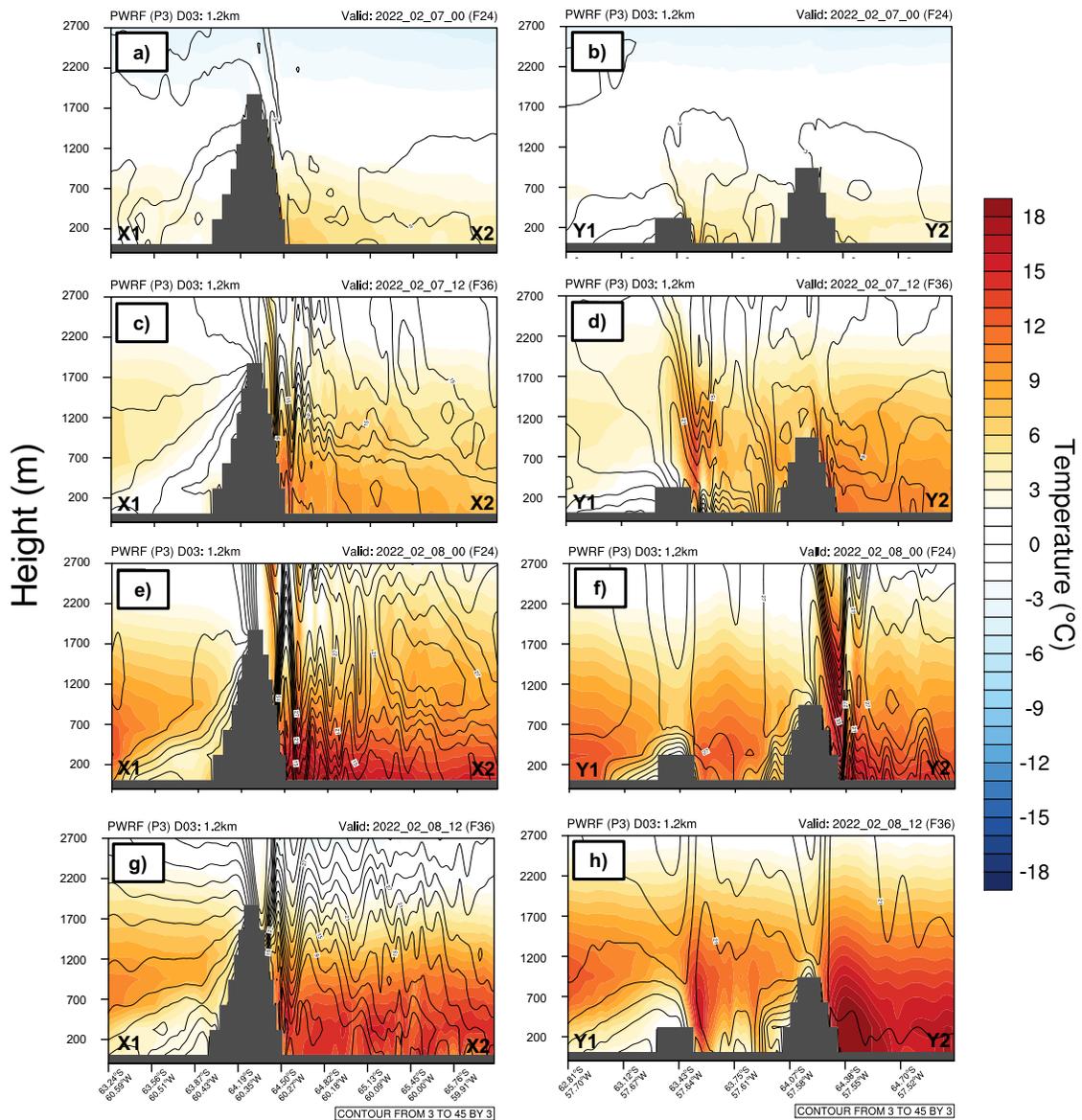
431 variable, and PWRF has updated this area as open water via REMA dataset. Further analysis  
 432 is needed to explain this difference.



433 **Figure 5.** 2m temperature and 10m wind field from ERA5 reanalysis data and PWRF  
 434 simulations at 0000UTC 07 February 2022 (a, b); 1200UTC 07 February 2022 (c, d);  
 435 0000UTC 08 February 2022 (e, f); and 1200UTC 08 February 2022 (g, h). All coastline  
 436 information is from the REMA topography dataset. ERA5 land-sea mask contains the  
 437 fraction of land within every grid box. Over Antarctica, it is defined by RAMP-2 dataset,  
 438 which does not include the 2002 Larsen B Ice Shelf collapse  
 439 (<https://confluence.ecmwf.int/pages/viewpage.action?pageId=208482147>).  
 440  
 441

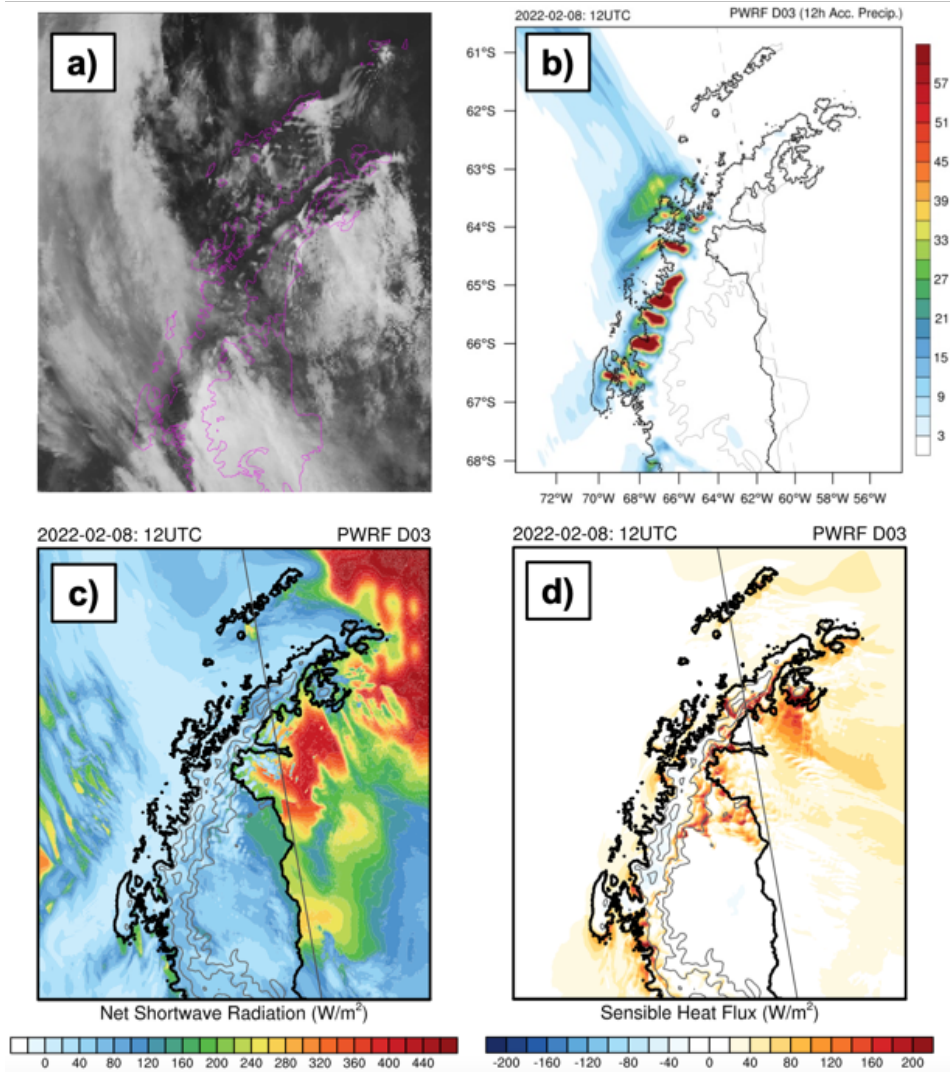
442 The cross-section of temperature and wind speed confirms the strong foehn warming  
 443 (Figs. 6, S7b and S7d). Temperature inversions were observed on the upwind side, with a  
 444 warm core  $\sim 700\text{m}$  above the surface, and intense mountain waves were captured on the  
 445 leeside (e.g., Fig. 6g). Such temperature inversions reflect a more-stratified atmosphere in the  
 446 2022 case, which could enhance low-level blocking on the upwind side, and adiabatic  
 447 warming on the leeside (Elvidge et al. 2015). However, the strong incoming wind brought by  
 448 ARs can force the low-level air to pass over the mountain peak (compensate for the low-level  
 449 blocking) and enhance the latent heat release on the upwind side. Furthermore, the strong  
 450 mountain waves on the leeside transfer sensible heat from the upper warm foehn flow to the

451 leeside surface of SCAR Inlet. The short-lived 2018 case, by contrast, has much weaker  
 452 mountain waves and more moderate foehn warming on the leeside (Figs. S5a, S6 and S7).  
 453 The foehn warming mainly affects the leeside of the James Ross Island and the mountain  
 454 base in the northern AP.



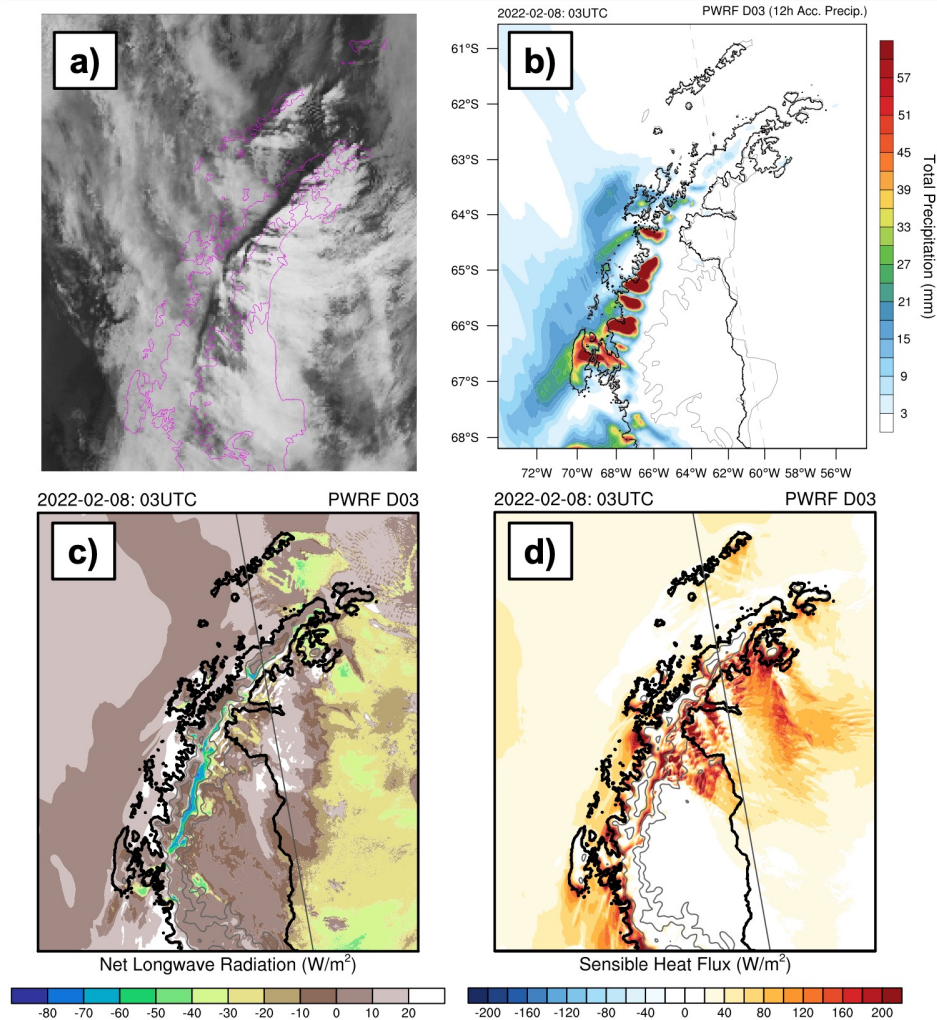
455  
 456 **Figure 6.** Vertical profiles of horizontal wind speed (horizontal only, u and v) and physical  
 457 temperature along cross-sections X1X2 (a, c, e, g) and Y1Y2 (b, d, f, h), at 0000UTC 07  
 458 February, 1200UTC 07 February, 0000UTC 08 February, and 1200UTC 08 February, 2022.  
 459 Cross-section X1X2 runs across the Graham Land, while cross-section Y1Y2 runs across the  
 460 Trinity Peninsula (Fig. 5).  
 461

462           The two major drivers of surface melting over SCAR Inlet were found to be strong  
463 SWD during reduced cloudiness due to foehn clearance and SHF transferred to the surface by  
464 the mountain waves. However, the main driver of surface melting was found to differ  
465 between daytime and nighttime. During the day, net shortwave radiation ( $SW_{net}$ ) is the  
466 leading contributor, ranging from 400 to 700  $Wm^{-2}$ . Sensible heat flux, as the secondary  
467 factor during the daytime, can reach up to 300  $Wm^{-2}$  (Fig. 7). During the night (Fig. 8), SHF  
468 maintains its strength, while the net shortwave radiation drops to 0  $Wm^{-2}$  (not shown). The  
469 SHF is strongly correlated with the magnitude of the foehn, while the  $SW_{net}$  is considerably  
470 more complicated. Also, the SHF exhibits a wave pattern for multiple time steps during the  
471 2022 event, especially closer to the mountain base (e.g., Figs. 7d and 8d). This pattern is  
472 consistent with mountain waves captured in the cross-section (Fig. 6) and cloud conditions  
473 from the Antarctic infrared composite (Fig. 7a) and MODIS corrected reflectance image  
474 (Figs. S8c and S8d).



475  
476  
477  
478  
479  
480

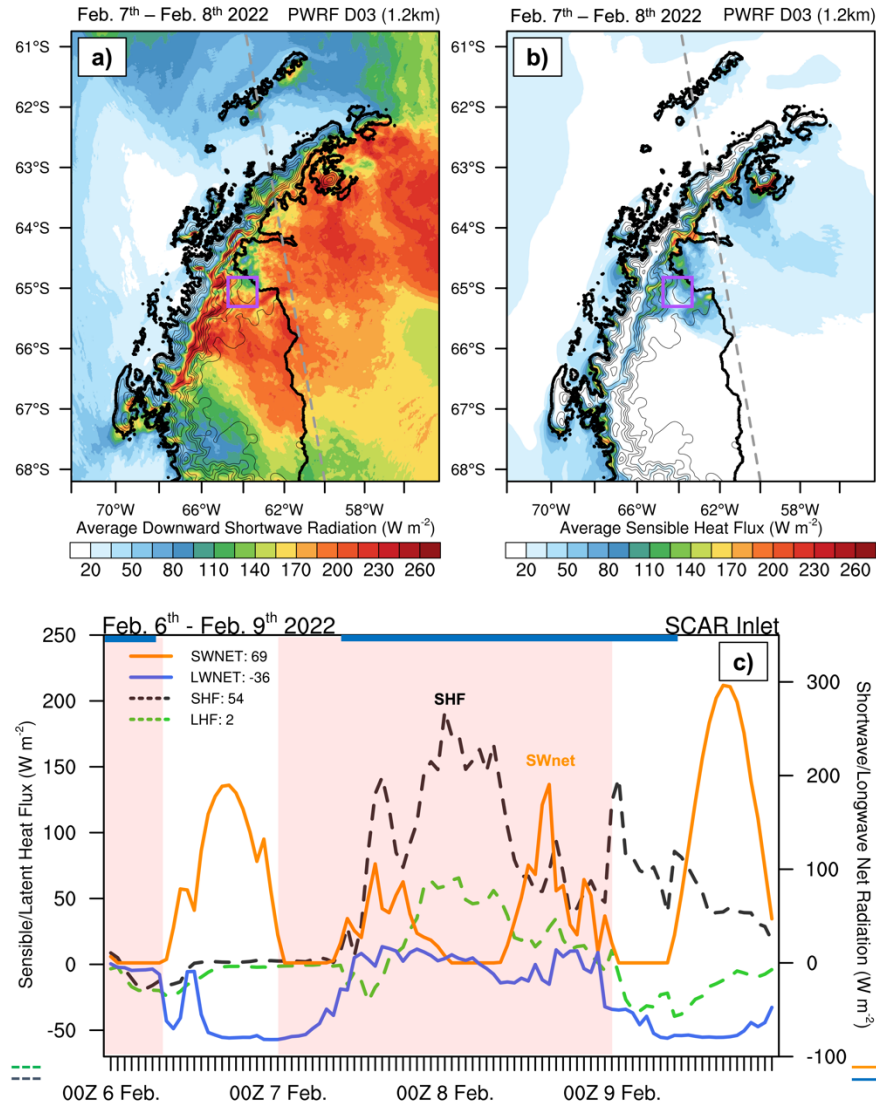
**Figure 7.** Clouds, precipitation, and the surface energy balance during the daytime, at 12UTC on 2022/02/08. a) Cloud cover from Antarctic composite infrared data. b) 12-h accumulated precipitation (00UTC - 12UTC) from PWRF d03. c) Net shortwave radiation from PWRF D03. d) Sensible heat flux from PWRF d03. Grey lines are meridians.



481  
 482 **Figure 8.** Surface energy balance pattern and cloud condition during the nighttime. a) Cloud  
 483 cover from Antarctic composite infrared data b) 12-h accumulated precipitation (1500UTC  
 484 07 - 0300UTC 08 February 2022) from PWRF d03. c) Net longwave radiation at 0300UTC  
 485 08 February 2022 from PWRF d03. d) Sensible heat flux at 0300UTC 08 February 2022  
 486 from PWRF d03.  
 487

488 During the 2022 case, weak low-level blocking and intense precipitation on the  
 489 upwind side can lead to clear sky and stronger foehn warming on the leeside (e.g., Figs. 7a,  
 490 and S8d). However, there is a gap between Trinity Peninsula and Joinville Island, which  
 491 allows moist marine air to reach the leeside and form clouds, especially low- and mid-level  
 492 liquid clouds (e.g., Figs. 7a and S9a). The foehn jets going through the lower elevation in  
 493 Graham Land can also transport extra moisture. When foehn warming is powered by the AR,

494 the moisture transport can be strong through those gaps. Thus, the foehn clearance can be  
495 compensated for by clouds formed from the moisture in the gap flows; given that cloud  
496 conditions can vary significantly with time (Fig. S8), the resulting SWD can be highly  
497 varying. Similar enhanced cloud impacts on the leeside were observed for the 2018 case.  
498 Taking SCAR Inlet as an example, the  $SW_{net}$  (average  $69 \text{ Wm}^{-2}$ ) contributes  $\sim 1.3$  times as  
499 much as the SHF (average  $54 \text{ Wm}^{-2}$ ) to the surface melting/warming from 00UTC 6 February  
500 to 23UTC 9 February (Fig. 9). The maximum of the SHF occurs on 03UTC 8 February,  
501 which is around the foehn peak (Fig. 9c). Orographic lee waves on the leeside transfer the  
502 sensible heat from upper foehn flow to the surface.

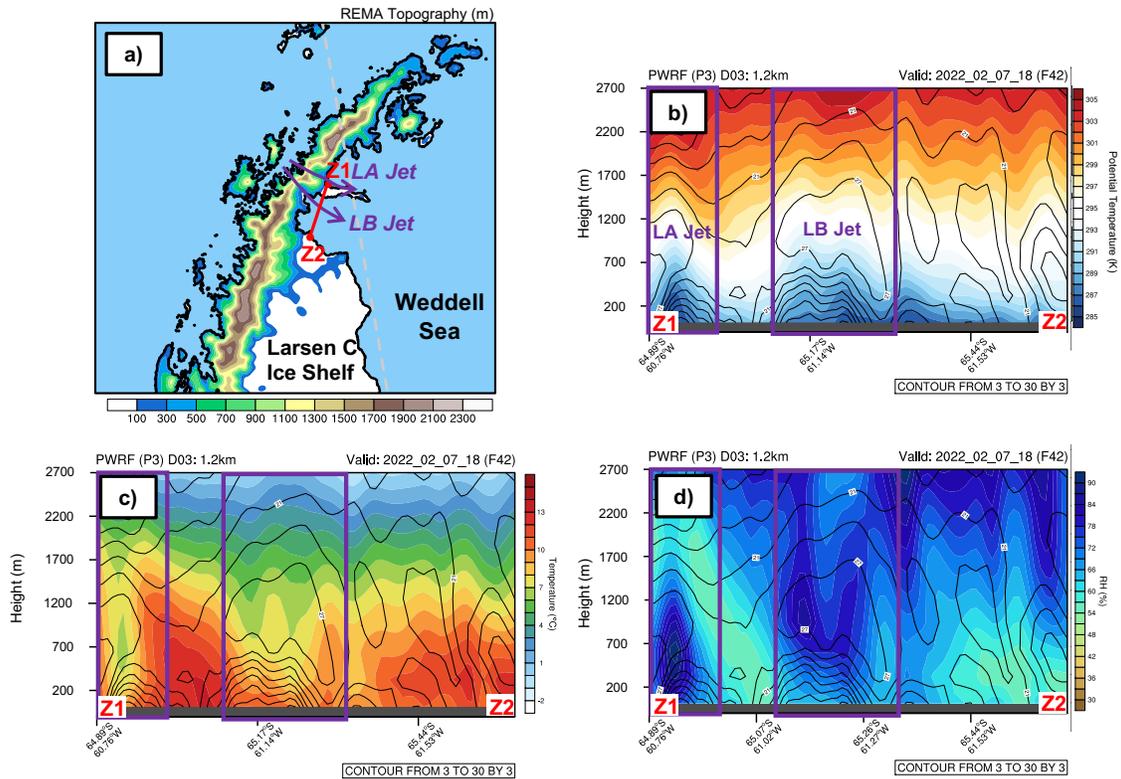


503 **Figure 9.** Surface energy balance during the peak of 2022 foehn event over the SCAR Inlet.  
 504 a) average downward shortwave radiation from hourly PWRF d03 simulations. a) average  
 506 average sensible heat flux from hourly PWRF d03 simulations. c) time series of net  
 507 shortwave/longwave radiation and sensible/latent heat flux within the purple box in a) and b).  
 508 Pink shadow indicates the foehn period and navy lines at the top of c) indicate the  
 509 atmospheric river effects over the SCAR Inlet.  
 510

511 Overall,  $SW_{net}$  is the major contributor to the surface warming over most of the ice  
 512 surface on the leeside, except the mountain base or areas strongly affected by the cloud  
 513 formation, where the SHF has an equal impact as  $SW_{net}$  (both  $\sim 140 \text{ W m}^{-2}$ ; Fig. 9). The  
 514 dominant contribution of  $SW_{net}$  after the foehn event mainly comes from stronger SWD with

515 time due to clear sky conditions (Fig. S8e). The combined AR/Foehn event can be more  
516 complicated due to the extra moisture input via dampened foehn effect over lower elevation  
517 regions (e.g., foehn jets) and potential cloud formation accordingly (Figs. S8 and S10).

518 Consistent with Laffin et al. (2022), two foehn jets were found over Larsen A and B  
519 in high-resolution PWRP outputs during the 2022 event (LA jet and LB jet, Fig. 10a). With  
520 faster wind speed, lower temperature, and higher relative humidity during the foehn jets  
521 (purple boxes in Figs. 10b - d) compared to the background air, the two jets created a cooling  
522 gap between the two warming spots mentioned before (Fig. 5). The maximum wind speed of  
523 the jets occurs at ~700m above the surface (Fig. 10b). Because the direction of the marine air  
524 advection varies with time, the locations of the jets shift slightly. For instance, the LB jet can  
525 affect either the Larsen B or SCAR Inlet depending on the incoming flow. Within the jets, a  
526 larger vertical potential temperature gradient indicates stronger sensible heat transfer from  
527 upper-level air to the surface (Fig. 10b). While temperatures and  $SW_{net}$  (due to the potential  
528 cloud formation) may be lower within foehn jets, the strong accompanying winds could  
529 accelerate the ice shelf disintegration via pushing ice to the ocean and enhancing SHF (Laffin  
530 et al. 2022; Elvidge et al. 2015). However, unlike Elvidge et al. (2015)'s foehn jet study over  
531 the Larsen C Ice shelf, where the surface was relatively smooth ice, both the LA and LB jets  
532 in 2022 blow over a surface that is a mixture of open water and floating ice (Fig. S8). Further  
533 research, such as trajectory analysis, is necessary to distinguish all the mechanisms that lead  
534 to surface warming.



535  
 536 **Figure 10.** Larsen A and B jet during the 2022 foehn case. a) illustrates the location of the  
 537 jets and the cross section (Z1Z2). b), c), d) Cross section of potential temperature,  
 538 temperature, and relative humidity (RH) with wind speed at 1800UTC 07 February 2022.  
 539 (LA jet: Larsen A jet. LB jet: Larsen B jet).  
 540

#### 541 4. Discussion

542 The maximum impact of foehn warming is expected to occur when the incoming  
 543 wind approaches the topographic barrier perpendicularly (e.g., during a zonal wind). Most of  
 544 the AP region, especially the southern area, will have a stronger foehn warming under the  
 545 zonal wind (Bozkurt et al. 2018). However, when there is a low over the Bellingshausen Sea  
 546 and a nearby blocking high over the Weddell Sea, the AP is more likely to experience  
 547 meridional warm air advection. Given that the northern tip of the AP tilts eastward, it will  
 548 experience a stronger foehn under a meridional (northerly) wind (Fig. S4). In other words,  
 549 the northern AP is more vulnerable to the combined impact from foehn and AR under a  
 550 persistent meridional wind, such as the 2022 case instead of the 2018 case. Also, the vertical

551 structure of the atmosphere on the upwind side also affects the foehn warming. A more  
552 stratified atmosphere with slow wind speed will result in a shallow foehn condition, which  
553 has low-level blocking on the upwind side and possible hydraulic jumps on the leeside  
554 (Durrán 1990). For example, the topographic blocking for the northerly meridional wind at  
555 850hPa persisted for 11 months during 2002-03 (Orr et al. 2004). In contrast, strong vertical  
556 wind shear and unstable atmosphere usually lead to intense orographic lifting on the upwind  
557 side and stationary orographic gravity wave on the leeside (Elvidge et al. 2015).

558 For the 2022 case, the strong AR brings faster and warmer moist air from the lower  
559 latitudes over the relatively colder ocean and propagates to the northern AP perpendicularly.  
560 On the upwind side, a temperature inversion is observed, as well as strong vertical wind  
561 shear due to the low-level jet (~700m above the surface; not shown). Thus, the 2022 case was  
562 characterized by weak low-level blocking and strong mountain waves on the leeside, which  
563 made this case closer to a deep foehn scenario. PWRP simulations show a weak-to-moderate  
564 hydraulic jump near the mountain peak and stationary mountain waves covering most of the  
565 leeside (e.g., Fig. 6g). By contrast, the 2015 case study conducted by Bozkurt et al. (2018)  
566 has strong low-level blocking on the upwind side (shallow foehn). Instead of the stationary  
567 orographic gravity wave, the leeside has a sharp and large hydraulic jump, which leads to the  
568 formation of “foehn gaps” (cloud-free zone) along the mountain base. Although shallow  
569 foehn often leads to a larger positive temperature anomaly via adiabatic warming (isentropic  
570 drawdown) and intensive SHF at the mountain base, deep foehn is more likely to result in  
571 extensive surface warming/melting via SHF from stationary orographic waves (Elvidge et al.  
572 2015). The direction and magnitude of AR can complicate the foehn warming via  
573 contributing extra moisture and also affect the atmospheric structure on the upwind side,

574 which is related to the development of mountain waves on the leeside. This will impact the  
575 SHF and cloud conditions, and the surface warming consequently.

576 Similar to the AP region, the eastern Ross Ice Shelf over WA experienced the  
577 combined impact of AR and foehn in a few historic surface melting events. With a blocking  
578 high (over the Bellingshausen/Amundsen Sea) and a nearby low-pressure system (over the  
579 Amundsen/Ross Sea), coastal WA is more likely to have strong warm marine air advection  
580 or ARs (Scott et al. 2019; Zou et al. 2021a). The eastern RIS on the leeside can have foehn  
581 warming subsequently. The local topography over the AP is different from WA. Instead of  
582 two relatively gentle mountain ranges (over Marie Byrd Land and Edward VII Land), the AP  
583 has one sharp topographic barrier along Graham Land. Thus, the AP usually has stronger  
584 foehn warming. In addition, both the AP and eastern RIS can experience foehn clearance and  
585 have direct moisture input that potentially led to cloud formation simultaneously. For  
586 example, during a 2015 melt event (Ghiz et al. 2021), Siple Dome had a descending warm  
587 and dry air mass that might have reduced the optical thickness of the clouds and enhanced  
588 all-wave radiation. In the 2022 case, cloud formation on the leeside triggered by the extra  
589 moisture via AR and gap flows hampers the SWD at the mountain base but increases the  
590 LWD slightly. Although the LA and LB jets reduce temperatures and the impacts from  
591  $SW_{net}$ , they could accelerate the ice shelf disintegration via pushing ice to the ocean and  
592 enhancing SHF (Fig. 10). The occurrence of AR and complicated local topography introduce  
593 more uncertainties to foehn studies over the AP.

594 The detailed mechanisms of foehn for both regions need to be analyzed case by case.  
595 With a colder background temperature, the RIS is at a lower risk of collapsing or intense  
596 surface melting. The RIS might experience moderate surface melting during a foehn event in

597 austral summer, and no melt ponding has been reported over the Siple Coast region (Ghiz et  
598 al. 2021; Zou et al. 2021b). In contrast, foehn/AR events contributed to the collapse of  
599 Larsen A Ice shelf in 1995 and Larsen B Ice Shelf in 2002 (Wille et al. 2022). An increasing  
600 AR frequency over the AP may occur in the future under climate change, as well as the  
601 positive SAM trend (Wille et al. 2021; Espinoza et al. 2018). Consequently, more intense and  
602 complicated foehn cases may occur, which can lead to extreme weather, such as record-  
603 breaking temperature and intense precipitation (e.g., Bozkurt et al. 2018; Gorodetskaya et al.,  
604 2022; González-Herrero et al. 2022). In addition, the fast-changing surface due to the melting  
605 and ice loss challenges the ability of numerical weather models to accurately describe surface  
606 condition, such as temperature. A more advanced land surface model that can accurately  
607 represent the changing surface dynamically (e.g., albedo and land mass) should be included  
608 in PWRP, especially for simulations over the AP region (e.g., Fig. S1). Field observations of  
609 cloud properties are needed to help validate model cloud microphysics, as well as its impact  
610 on surface warming.

611

## 612 **5. Summary**

613 The AP region experienced a combined impact from AR and foehn warming during  
614 both 2018 and 2022 cases. With a blocking high located at the Weddell Sea during the 2022  
615 case, the northern tip of the AP is hit by a northwesterly AR perpendicularly for three days.  
616 Thus, compared to the 2018 case, the 2022 case was characterized by stronger and longer-  
617 lasting foehn warming. Over the Larsen B embayment during the 2022 foehn case, there was  
618 an average 2m temperature increase of 5 °C within 24 hours. A low-pressure center to the  
619 west of the AP with a blocking high to the east often leads to a stationary circulation pattern,

620 which contributes to poleward moisture transport (Wang et al. 2022b). The importance of the  
621 blocking high to the regional circulation over the AP as well as the rest of the Antarctic  
622 continent has been highlighted in multiple research papers. It not only enhances the pressure  
623 gradient and accelerates the marine air advection (AR related), but the blocking high also  
624 creates a more persistent pattern that results in a longer-lasting event, especially for the  
625 northern AP (e.g., Hirasawa et al. 2013; Nicolas et al. 2017; Xu et al. 2021).

626 The persistent impact of the AR can lead to strong foehn warming along the leeside  
627 of the AP, especially from the latent heat release on the upwind side (Bozkurt et al. 2018;  
628 Wille et al. 2022). Both 2018 (ENSO-neutral) and 2022 (La Niña) cases have intense  
629 precipitation on the western AP, and warm downslope wind on the eastern side. As a deep-  
630 foehn like case, the 2022 event has strong stationary orographic gravity waves on the leeside,  
631 which enhances heat transfer between the upper foehn flow and the surface (Fig. 6). The  
632 2022 case has two warming spots, one over the Larsen B embayment and the other on the  
633 leeside of James Ross Island (Fig. 5). Between these two spots, there is a relatively cooler  
634 gap close to Robertson Island, which is indicative of a strong foehn jet (the LB jet).

635 During the austral summer, the AP region experiences a strong diurnal cycle. Thus,  
636 the lead driver of surface warming is different between daytime and nighttime (Figs. 7 and  
637 8). During the daytime,  $SW_{net}$  significantly contributes to the surface warming/melting over  
638 the SCAR Inlet, followed by the SHF. During the nighttime, SHF is the major driver.  
639 Shortwave radiation is associated with foehn clearance, which can be amplified by the AR  
640 intrusion. However, in the 2022 case, gap flows/foehn jets significantly contribute to  
641 moisture transports on the leeside and reduce  $SW_{net}$ , especially at the mountain base. On the  
642 other hand, SHF continuously contributes to surface warming, which is highly correlated

643 with the magnitude of the foehn. Overall,  $SW_{net}$  is the major contributor to surface  
644 warming/melting over the ice surface during the 2022 foehn period, except for the mountain  
645 base where SHF has an equal contribution or areas with cloud formation due to the gap  
646 flows/foehn jets.

647 In general, the AR intrusion complicates the foehn warming over the AP region, and  
648 usually amplifies the surface warming/melting. First, ARs with longer duration usually  
649 propagate towards the AP in a meridional direction, which moves perpendicular to the  
650 northern tip but not to the southern AP. Thus, the Larsen C ice shelf will have less foehn  
651 warming, but Larsen A and B (including SCAR Inlet) will be under greater impact. Second,  
652 there are several gaps along the topographic barrier over the AP, especially over the northern  
653 tip. Foehn jets via the low-elevation gap can compensate for the increased SWD resulting  
654 from foehn clearance and enhance the SHF. Third, for the 2022 case, SWD is the leading  
655 driver for the surface warming over the ice surface with SHF playing a significant role.  
656 However, the mechanisms of AR/foehn warming events over the AP vary case by case. ARs  
657 can amplify the leeside foehn warming via increased latent heat release on the upwind but  
658 can also hamper the foehn clearance via potential cloud formation. Depending on the phase,  
659 height, and thickness of clouds on the leeside, the net radiation can be different. All cases  
660 need to be analyzed independently and trajectory analysis will help distinguish the impact of  
661 each driver. Our future research will 1) continue to improve the high-resolution simulations  
662 over the AP region; 2) improve our understanding of the relationship of AR and foehn under  
663 different synoptic circulation patterns; 3) quantify the contribution of each driver to surface  
664 warming in order to build a better understanding of surface melting over the AP under the  
665 influence of climate change.

**666 Acknowledgments**

667 This collaborative research was supported by National Science Foundation (NSF) grants  
668 2127632, 2229392 and FIRO2 W912HZ-19-2-0023 (U.S. Army Corps of Engineers). I.V.G.  
669 thanks the support by the strategic funding to CESAM (grant nos. UIDP/50017/2020,  
670 UIDB/50017/2020, and LA/P/0094/2020), to CIIMAR (UIDB/04423/2020, UIDP/04423/2020),  
671 2021.03140.CEECIND and Project ATLACE (CIRCNA/CAC/0273/2019) through national  
672 funds provided by FCT – Fundação para a Ciência e a Tecnologia. D.H.B. acknowledges support  
673 from NSF grant 2205398. M.A.L. acknowledges support from NSF grants 1924730, 1951603,  
674 1951720. J.D.W. acknowledges support from the Agence Nationale de la Recherche projects  
675 ANR-20-CE01-0013 (ARCA). R.R.C. thanks the support of INACH (Preis RT\_69-20) and  
676 ANID (Preis FONDECYT 1191932 & ANILLO ACT210046). The Polar WRF model is  
677 developed and is maintained by the Polar Meteorology Group, Byrd Polar and Climate Research  
678 Center (BPCRC), The Ohio State University. Contribution number 1607 of BPCRC. Polar WRF  
679 simulations were performed on the San Diego Supercomputing Center’s COMET resource  
680 through AR Program, Phase II 460001361 and III 4600014294 (State of California, Department  
681 of Water Resources). We are grateful to the Instituto Antartica Argentino (IAA/DNA), the  
682 Servicio Meteorologico Nacional (SMN), the Integrated Global Radiosonde Archive for  
683 radiosonde and surface meteorological data from Marambio Station, the Dirección  
684 Meteorológica de Chile (DMC), and to the Instituto Antartico Chileno (INACH) for supporting  
685 observations in the Antarctic Peninsula. We also want to thank Diego Campos and Edgardo  
686 Sepulveda for radiosonde measurements.

687 **Open Research**

688 ERA5 and ERA5 Land reanalysis data are available at Copernicus Climate Change Service  
689 (C3S) Climate Data Store. Surface station observations and Antarctic composite infrared satellite  
690 imagery data are available at Antarctic Meteorological Research and Data Center (AMRDC)  
691 (<https://amrdcdata.ssec.wisc.edu/>). The Worldview tool from NASA's Earth Observing System  
692 Data and Information System (EOSDIS) provides additional satellite imagery  
693 (<https://worldview.earthdata.nasa.gov/>). Moderate Resolution Imaging Spectroradiometer  
694 (MODIS) albedo is produced by the National Aeronautics and Space Administration (NASA;  
695 <https://lpdaac.usgs.gov/products/mcd43c3v006/>). Reference Elevation Model of Antarctica  
696 (REMA) topography used in PWRF is available at [https://www.envidat.ch/dataset/rema-](https://www.envidat.ch/dataset/rema-topography-and-antarcticalc2000-for-wrf)  
697 [topography-and-antarcticalc2000-for-wrf](https://www.envidat.ch/dataset/rema-topography-and-antarcticalc2000-for-wrf). PWRF model is available upon request at Polar  
698 Meteorology Group, Byrd Polar and Climate Research Center, The Ohio State University.  
699

700 **References:**

- 701 Bodas-Salcedo, A., P. G. Hill, K. Furtado, K. D. Williams, P. R. Field, J. C. Manners, P. Hyder,  
702 and S. Kato, 2016: Large Contribution of Supercooled Liquid Clouds to the Solar  
703 Radiation Budget of the Southern Ocean. *Journal of Climate*, **29**, 4213–4228,  
704 <https://doi.org/10.1175/JCLI-D-15-0564.1>.
- 705 Bozkurt, D., R. Rondanelli, J. C. Marín, and R. Garreaud, 2018: Foehn Event Triggered by an  
706 Atmospheric River Underlies Record-Setting Temperature Along Continental Antarctica.  
707 *Journal of Geophysical Research: Atmospheres*, **123**, 3871–3892,  
708 <https://doi.org/10.1002/2017JD027796>.
- 709 van den Broeke, M., 2005: Strong surface melting preceded collapse of Antarctic Peninsula ice  
710 shelf. *Geophysical Research Letters*, **32**, <https://doi.org/10.1029/2005GL023247>.
- 711 Bromwich, D. H., F. O. Otieno, K. M. Hines, K. W. Manning, and E. Shilo, 2013:  
712 Comprehensive evaluation of polar weather research and forecasting model performance  
713 in the Antarctic. *Journal of Geophysical Research: Atmospheres*, **118**, 274–292,  
714 <https://doi.org/10.1029/2012JD018139>.
- 715 ———, and Coauthors, 2020: The Year of Polar Prediction in the Southern Hemisphere (YOPP-  
716 SH). *Bulletin of the American Meteorological Society*, **101**, E1653–E1676,  
717 <https://doi.org/10.1175/BAMS-D-19-0255.1>.
- 718 Chyhareva, A., I. Gorodetskaya, S. Krakovska, D. Pishniak, and P. Rowe, 2021: Precipitation  
719 phase transition in austral summer over the Antarctic Peninsula. *Ukrainian Antarctic*  
720 *journal*, 32–46, <https://doi.org/10.33275/1727-7485.1.2021.664>.

- 721 Clem, K. R., J. A. Renwick, J. McGregor, and R. L. Fogt, 2016: The relative influence of ENSO  
722 and SAM on Antarctic Peninsula climate. *Journal of Geophysical Research:*  
723 *Atmospheres*, **121**, 9324–9341, <https://doi.org/10.1002/2016JD025305>.
- 724 ———, D. Bozkurt, D. Kennett, J. C. King, and J. Turner, 2022: Central tropical Pacific  
725 convection drives extreme high temperatures and surface melt on the Larsen C Ice Shelf,  
726 Antarctic Peninsula. *Nature Communications*, **13**, 3906, [https://doi.org/10.1038/s41467-](https://doi.org/10.1038/s41467-022-31119-4)  
727 [022-31119-4](https://doi.org/10.1038/s41467-022-31119-4).
- 728 Clough, S. A., M. W. Shephard, E. J. Mlawer, J. S. Delamere, M. J. Iacono, K. Cady-Pereira, S.  
729 Boukabara, and P. D. Brown, 2005: Atmospheric radiative transfer modeling: a summary  
730 of the AER codes. *Journal of Quantitative Spectroscopy and Radiative Transfer*, **91**,  
731 233–244, <https://doi.org/10.1016/j.jqsrt.2004.05.058>.
- 732 Corbea-Pérez, A., J. F. Calleja, C. Recondo, and S. Fernández, 2021: Evaluation of the MODIS  
733 (C6) Daily Albedo Products for Livingston Island, Antarctic. *Remote Sensing*, **13**, 2357,  
734 <https://doi.org/10.3390/rs13122357>.
- 735 Davis, S. M., and Coauthors, 2017: Assessment of upper tropospheric and stratospheric water  
736 vapor and ozone in reanalyses as part of S-RIP. *Atmospheric Chemistry and Physics*, **17**,  
737 12743–12778, <https://doi.org/10.5194/acp-17-12743-2017>.
- 738 Durran, D. R., 1990: Mountain Waves and Downslope Winds. *Atmospheric Processes over*  
739 *Complex Terrain*, R.M. Banta et al., Eds., *Meteorological Monographs*, American  
740 Meteorological Society, 59–81.
- 741 Elvidge, A. D., and I. A. Renfrew, 2016: The Causes of Foehn Warming in the Lee of  
742 Mountains. *Bulletin of the American Meteorological Society*, **97**, 455–466,  
743 <https://doi.org/10.1175/BAMS-D-14-00194.1>.

- 744 ———, ———, J. C. King, A. Orr, T. A. Lachlan-Cope, M. Weeks, and S. L. Gray, 2015: Foehn jets  
745 over the Larsen C Ice Shelf, Antarctica. *Quarterly Journal of the Royal Meteorological*  
746 *Society*, **141**, 698–713, <https://doi.org/10.1002/qj.2382>.
- 747 ———, P. Kuipers Munneke, J. C. King, I. A. Renfrew, and E. Gilbert, 2020: Atmospheric Drivers  
748 of Melt on Larsen C Ice Shelf: Surface Energy Budget Regimes and the Impact of Foehn.  
749 *Journal of Geophysical Research: Atmospheres*, **125**, e2020JD032463,  
750 <https://doi.org/10.1029/2020JD032463>.
- 751 Espinoza, V., D. E. Waliser, B. Guan, D. A. Lavers, and F. M. Ralph, 2018: Global Analysis of  
752 Climate Change Projection Effects on Atmospheric Rivers. *Geophysical Research*  
753 *Letters*, **45**, 4299–4308, <https://doi.org/10.1029/2017GL076968>.
- 754 Feron, S., R. R. Cordero, A. Damiani, A. Malhotra, G. Seckmeyer, and P. Llanillo, 2021:  
755 Warming events projected to become more frequent and last longer across Antarctica.  
756 *Scientific Reports*, **11**, 19564, <https://doi.org/10.1038/s41598-021-98619-z>.
- 757 Gerber, F. and M. Lehning, 2020: REMA topography and AntarcticaLC2000 for WRF. EnviDat.  
758 <https://doi.org/10.16904/envidat.190>.
- 759 Ghiz, M. L., R. C. Scott, A. M. Vogelmann, J. T. M. Lenaerts, M. Lazzara, and D. Lubin, 2021:  
760 Energetics of surface melt in West Antarctica. *The Cryosphere*, **15**, 3459–3494,  
761 <https://doi.org/10.5194/tc-15-3459-2021>.
- 762 González-Herrero, S., D. Barriopedro, R. M. Trigo, J. A. López-Bustins, and M. Oliva, 2022:  
763 Climate warming amplified the 2020 record-breaking heatwave in the Antarctic  
764 Peninsula. *Communications Earth and Environment*, **3**, 122,  
765 <https://doi.org/10.1038/s43247-022-00450-5>.

- 766 Gorodetskaya, I. V., T. Silva, H. Schmithüsen, and N. Hirasawa, 2020: Atmospheric River  
767 Signatures in Radiosonde Profiles and Reanalyses at the Dronning Maud Land Coast,  
768 East Antarctica. *Advances in Atmospheric Sciences*, **37**, 455–476,  
769 <https://doi.org/10.1007/s00376-020-9221-8>.
- 770 ———, and Coauthors, 2022: Compound drivers behind new record high temperatures and surface  
771 melt at the Antarctic Peninsula in February 2022: tropical Pacific convection,  
772 atmospheric river and foehn. *Communications Earth and Environment*. In preparation.
- 773 Hersbach, H., and Coauthors, 2020: The ERA5 global reanalysis. *Quarterly Journal of the Royal*  
774 *Meteorological Society*, **146**, 1999–2049, <https://doi.org/10.1002/qj.3803>.
- 775 Hines, K. M., and D. H. Bromwich, 2008: Development and Testing of Polar Weather Research  
776 and Forecasting (WRF) Model. Part I: Greenland Ice Sheet Meteorology. *Monthly*  
777 *Weather Review*, **136**, 1971–1989, <https://doi.org/10.1175/2007MWR2112.1>.
- 778 ———, ———, S.-H. Wang, I. Silber, J. Verlinde, and D. Lubin, 2019: Microphysics of summer  
779 clouds in central West Antarctica simulated by the Polar Weather Research and  
780 Forecasting Model (WRF) and the Antarctic Mesoscale Prediction System (AMPS).  
781 *Atmospheric Chemistry and Physics*, **19**, 12431–12454, [https://doi.org/10.5194/acp-19-](https://doi.org/10.5194/acp-19-12431-2019)  
782 [12431-2019](https://doi.org/10.5194/acp-19-12431-2019).
- 783 ———, ———, I. Silber, L. M. Russell, and L. Bai, 2021: Predicting Frigid Mixed-Phase Clouds for  
784 Pristine Coastal Antarctica. *Journal of Geophysical Research: Atmospheres*, **126**,  
785 [e2021JD035112](https://doi.org/10.1029/2021JD035112), <https://doi.org/10.1029/2021JD035112>.
- 786 Hirasawa, N., H. Nakamura, H. Motoyama, M. Hayashi, and T. Yamanouchi, 2013: The role of  
787 synoptic-scale features and advection in prolonged warming and generation of different  
788 forms of precipitation at Dome Fuji station, Antarctica, following a prominent blocking

- 789 event. *Journal of Geophysical Research: Atmospheres*, **118**, 6916–6928,  
790 <https://doi.org/10.1002/jgrd.50532>.
- 791 Hoffmann, L., and Coauthors, 2019: From ERA-Interim to ERA5: the considerable impact of  
792 ECMWF’s next-generation reanalysis on Lagrangian transport simulations. *Atmospheric  
793 Chemistry and Physics*, **19**, 3097–3124, <https://doi.org/10.5194/acp-19-3097-2019>.
- 794 Holland, P. R., H. F. J. Corr, H. D. Pritchard, D. G. Vaughan, R. J. Arthern, A. Jenkins, and M.  
795 Tedesco, 2011: The air content of Larsen Ice Shelf. *Geophysical Research Letters*, **38**,  
796 <https://doi.org/10.1029/2011GL047245>.
- 797 Howat, I. M., C. Porter, B. E. Smith, M.-J. Noh, and P. Morin, 2019: The Reference Elevation  
798 Model of Antarctica. *The Cryosphere*, **13**, 665–674, [https://doi.org/10.5194/tc-13-665-](https://doi.org/10.5194/tc-13-665-2019)  
799 2019.
- 800 Jakobs, C. L., C. H. Reijmer, M. R. van den Broeke, W. J. van de Berg, and J. M. van Wessem,  
801 2021: Spatial Variability of the Snowmelt-Albedo Feedback in Antarctica. *Journal of  
802 Geophysical Research: Earth Surface*, **126**, e2020JF005696,  
803 <https://doi.org/10.1029/2020JF005696>.
- 804 Jones, M. E., D. H. Bromwich, J. P. Nicolas, J. Carrasco, E. Plavcová, X. Zou, and S.-H. Wang,  
805 2019: Sixty Years of Widespread Warming in the Southern Middle and High Latitudes  
806 (1957–2016). *Journal of Climate*, **32**, 6875–6898, [https://doi.org/10.1175/JCLI-D-18-](https://doi.org/10.1175/JCLI-D-18-0565.1)  
807 0565.1.
- 808 Kain, J. S., 2004: The Kain–Fritsch Convective Parameterization: An Update. *Journal of Applied  
809 Meteorology and Climatology*, **43**, 170–181, [https://doi.org/10.1175/1520-](https://doi.org/10.1175/1520-0450(2004)043<0170:TKCPAU>2.0.CO;2)  
810 0450(2004)043<0170:TKCPAU>2.0.CO;2.

- 811 Laffin, M. K., C. S. Zender, M. van Wessem, and S. Marinsek, 2022: The role of föhn winds in  
812 eastern Antarctic Peninsula rapid ice shelf collapse. *The Cryosphere*, **16**, 1369–1381,  
813 <https://doi.org/10.5194/tc-16-1369-2022>.
- 814 Lazzara, M. A., G. A. Weidner, L. M. Keller, J. E. Thom, and J. J. Cassano, 2012: Antarctic  
815 Automatic Weather Station Program: 30 Years of Polar Observation. *Bulletin of the*  
816 *American Meteorological Society*, **93**, 1519–1537, [https://doi.org/10.1175/BAMS-D-11-](https://doi.org/10.1175/BAMS-D-11-00015.1)  
817 [00015.1](https://doi.org/10.1175/BAMS-D-11-00015.1).
- 818 Listowski, C., and T. Lachlan-Cope, 2017: The microphysics of clouds over the Antarctic  
819 Peninsula – Part 2: modelling aspects within Polar WRF. *Atmospheric Chemistry and*  
820 *Physics*, **17**, 10195–10221, <https://doi.org/10.5194/acp-17-10195-2017>.
- 821 —, J. Delanoë, A. Kirchgaessner, T. Lachlan-Cope, and J. King, 2019: Antarctic clouds,  
822 supercooled liquid water and mixed phase, investigated with DARDAR: geographical  
823 and seasonal variations. *Atmospheric Chemistry and Physics*, **19**, 6771–6808,  
824 <https://doi.org/10.5194/acp-19-6771-2019>.
- 825 Luckman, A., A. Elvidge, D. Jansen, B. Kulesa, P. K. Munneke, J. King, and N. E. Barrand,  
826 2014: Surface melt and ponding on Larsen C Ice Shelf and the impact of föhn winds.  
827 *Antarctic Science*, **26**, 625–635, <https://doi.org/10.1017/S0954102014000339>.
- 828 Marshall, G. J., 2003: Trends in the Southern Annular Mode from Observations and Reanalyses.  
829 *Journal of Climate*, **16**, 4134–4143, [https://doi.org/10.1175/1520-](https://doi.org/10.1175/1520-0442(2003)016<4134:TITSAM>2.0.CO;2)  
830 [0442\(2003\)016<4134:TITSAM>2.0.CO;2](https://doi.org/10.1175/1520-0442(2003)016<4134:TITSAM>2.0.CO;2).
- 831 —, A. Orr, N. P. M. van Lipzig, and J. C. King, 2006: The Impact of a Changing Southern  
832 Hemisphere Annular Mode on Antarctic Peninsula Summer Temperatures. *Journal of*  
833 *Climate*, **19**, 5388–5404, <https://doi.org/10.1175/JCLI3844.1>.

- 834 Mattingly, K. S., T. L. Mote, X. Fettweis, D. van As, K. V. Tricht, S. Lhermitte, C. Pettersen,  
835 and R. S. Fausto, 2020: Strong Summer Atmospheric Rivers Trigger Greenland Ice Sheet  
836 Melt through Spatially Varying Surface Energy Balance and Cloud Regimes. *Journal of*  
837 *Climate*, **33**, 6809–6832, <https://doi.org/10.1175/JCLI-D-19-0835.1>.
- 838 Mulvaney, R., and Coauthors, 2012: Recent Antarctic Peninsula warming relative to Holocene  
839 climate and ice-shelf history. *Nature*, **489**, 141–144, <https://doi.org/10.1038/nature11391>.
- 840 Muñoz-Sabater, J., and Coauthors, 2021: ERA5-Land: a state-of-the-art global reanalysis dataset  
841 for land applications. *Earth System Science Data*, **13**, 4349–4383,  
842 <https://doi.org/10.5194/essd-13-4349-2021>.
- 843 Nakanishi, M., and H. Niino, 2006: An Improved Mellor–Yamada Level-3 Model: Its Numerical  
844 Stability and Application to a Regional Prediction of Advection Fog. *Boundary-Layer*  
845 *Meteorol*, **119**, 397–407, <https://doi.org/10.1007/s10546-005-9030-8>.
- 846 NASA/LARC/SD/ASDC, 2017: CERES and GEO-Enhanced TOA, Within-Atmosphere and  
847 Surface Fluxes, Clouds and Aerosols 1-Hourly Terra-Aqua Edition4A. Available at:  
848 [https://doi.org/10.5067/TERRA+AQUA/CERES/SYN1DEG-1HOUR\\_L3.004A](https://doi.org/10.5067/TERRA+AQUA/CERES/SYN1DEG-1HOUR_L3.004A).
- 849 NASA – 2022 National Aeronautics and Space Administration. Larsen B Embayment Breaks Up  
850 (2020). [https://earthobservatory.nasa.gov/images/149410/larsen-b-embayment-breaks-](https://earthobservatory.nasa.gov/images/149410/larsen-b-embayment-breaks-up?utm_source=TWITTER&utm_medium=NASAEarth&utm_campaign=NASASocial&linkId=150596699)  
851 [up?utm\\_source=TWITTER&utm\\_medium=NASAEarth&utm\\_campaign=NASASocial&](https://earthobservatory.nasa.gov/images/149410/larsen-b-embayment-breaks-up?utm_source=TWITTER&utm_medium=NASAEarth&utm_campaign=NASASocial&linkId=150596699)  
852 [linkId=150596699](https://earthobservatory.nasa.gov/images/149410/larsen-b-embayment-breaks-up?utm_source=TWITTER&utm_medium=NASAEarth&utm_campaign=NASASocial&linkId=150596699). Accessed 31 October 2022.
- 853 Nicolas, J. P., and Coauthors, 2017: January 2016 extensive summer melt in West Antarctica  
854 favoured by strong El Niño. *Nature Communications*, **8**, 15799,  
855 <https://doi.org/10.1038/ncomms15799>.

- 856 Niu, G.-Y., and Coauthors, 2011: The community Noah land surface model with  
857 multiparameterization options (Noah-MP): 1. Model description and evaluation with  
858 local-scale measurements. *Journal of Geophysical Research: Atmospheres*, **116**,  
859 <https://doi.org/10.1029/2010JD015139>.
- 860 Orr, A., D. Cresswell, G. J. Marshall, J. C. R. Hunt, J. Sommeria, C. G. Wang, and M. Light,  
861 2004: A ‘low-level’ explanation for the recent large warming trend over the western  
862 Antarctic Peninsula involving blocked winds and changes in zonal circulation.  
863 *Geophysical Research Letters*, **31**, <https://doi.org/10.1029/2003GL019160>.
- 864 Paolo, F. S., H. A. Fricker, and L. Padman, 2015: Volume loss from Antarctic ice shelves is  
865 accelerating. *Science*, **348**, 327–331, <https://doi.org/10.1126/science.aaa0940>.
- 866 Powers, J. G., K. W. Manning, D. H. Bromwich, J. J. Cassano, and A. M. Cayette, 2012: A  
867 Decade of Antarctic Science Support Through Amps. *Bulletin of the American*  
868 *Meteorological Society*, **93**, 1699–1712, <https://doi.org/10.1175/BAMS-D-11-00186.1>.
- 869 Ralph, F. M., P. J. Neiman, and G. A. Wick, 2004: Satellite and CALJET Aircraft Observations  
870 of Atmospheric Rivers over the Eastern North Pacific Ocean during the Winter of  
871 1997/98. *Monthly Weather Review*, **132**, 1721–1745, [https://doi.org/10.1175/1520-0493\(2004\)132<1721:SACAOO>2.0.CO;2](https://doi.org/10.1175/1520-0493(2004)132<1721:SACAOO>2.0.CO;2).
- 873 ———, J. J. Rutz, J. M. Cordeira, M. Dettinger, M. Anderson, D. Reynolds, L. J. Schick, and C.  
874 Smallcomb, 2019: A Scale to Characterize the Strength and Impacts of Atmospheric  
875 Rivers. *Bulletin of the American Meteorological Society*, **100**, 269–289,  
876 <https://doi.org/10.1175/BAMS-D-18-0023.1>.

- 877 Rignot, E., G. Casassa, P. Gogineni, W. Krabill, A. Rivera, and R. Thomas, 2004: Accelerated  
878 ice discharge from the Antarctic Peninsula following the collapse of Larsen B ice shelf.  
879 *Geophysical Research Letters*, **31**, <https://doi.org/10.1029/2004GL020697>.
- 880 Rignot, E., J. Mouginot, B. Scheuchl, M. van den Broeke, M. J. van Wessem, and M.  
881 Morlighem, 2019: Four decades of Antarctic Ice Sheet mass balance from 1979–2017.  
882 *Proceedings of the National Academy of Sciences*, **116**, 1095–1103,  
883 <https://doi.org/10.1073/pnas.1812883116>.
- 884 Rott, H., P. Skvarca, and T. Nagler, 1996: Rapid Collapse of Northern Larsen Ice Shelf,  
885 Antarctica. *Science*, **271**, 788–792, <https://doi.org/10.1126/science.271.5250.788>.
- 886 Scambos, T. A., C. Hulbe, M. Fahnestock, and J. Bohlander, 2000: The link between climate  
887 warming and break-up of ice shelves in the Antarctic Peninsula. *Journal of Glaciology*,  
888 **46**, 516–530, <https://doi.org/10.3189/172756500781833043>.
- 889 Scott, R. C., J. P. Nicolas, D. H. Bromwich, J. R. Norris, and D. Lubin, 2019: Meteorological  
890 Drivers and Large-Scale Climate Forcing of West Antarctic Surface Melt. *Journal of*  
891 *Climate*, **32**, 665–684, <https://doi.org/10.1175/JCLI-D-18-0233.1>.
- 892 Schaaf, C. and Z. Wang, 2015: MCD43C3 MODIS/Terra+Aqua BRDF/Albedo Albedo Daily L3  
893 Global 0.05Deg CMG V006. 2015, distributed by NASA EOSDIS Land Processes  
894 DAAC.
- 895 Shepherd, A., and Coauthors, 2018: Mass balance of the Antarctic Ice Sheet from 1992 to 2017.  
896 *Nature*, **558**, 219–222, <https://doi.org/10.1038/s41586-018-0179-y>.
- 897 Siegert, M., and Coauthors, 2019: The Antarctic Peninsula Under a 1.5°C Global Warming  
898 Scenario. *Frontiers in Environmental Science*, **7**.  
899 <https://doi.org/10.3389/fenvs.2019.00102>.

- 900 Smith, B., and Coauthors, 2020: Pervasive ice sheet mass loss reflects competing ocean and  
901 atmosphere processes. *Science*, **368**, 1239–1242, <https://doi.org/10.1126/science.aaz5845>.
- 902 Terpstra, A., I. V. Gorodetskaya, and H. Sodemann, 2021: Linking Sub-Tropical Evaporation  
903 and Extreme Precipitation Over East Antarctica: An Atmospheric River Case Study.  
904 *Journal of Geophysical Research: Atmospheres*, **126**, e2020JD033617,  
905 <https://doi.org/10.1029/2020JD033617>.
- 906 Tetzner, D., E. Thomas, and C. Allen, 2019: A Validation of ERA5 Reanalysis Data in the  
907 Southern Antarctic Peninsula—Ellsworth Land Region, and Its Implications for Ice Core  
908 Studies. *Geosciences*, **9**, 289, <https://doi.org/10.3390/geosciences9070289>.
- 909 Tuckett, P. A., J. C. Ely, A. J. Sole, S. J. Livingstone, B. J. Davison, J. Melchior van Wessem,  
910 and J. Howard, 2019: Rapid accelerations of Antarctic Peninsula outlet glaciers driven by  
911 surface melt. *Nature Communications*, **10**, 4311, [https://doi.org/10.1038/s41467-019-](https://doi.org/10.1038/s41467-019-12039-2)  
912 [12039-2](https://doi.org/10.1038/s41467-019-12039-2).
- 913 Turton, J. V., A. Kirchgaessner, A. N. Ross, and J. C. King, 2018: The spatial distribution and  
914 temporal variability of föhn winds over the Larsen C ice shelf, Antarctica. *Quarterly*  
915 *Journal of the Royal Meteorological Society*, **144**, 1169–1178,  
916 <https://doi.org/10.1002/qj.3284>.
- 917 Wang, D., S. Liang, T. He, Y. Yu, C. Schaaf, and Z. Wang, 2015: Estimating daily mean land  
918 surface albedo from MODIS data. *Journal of Geophysical Research: Atmospheres*, **120**,  
919 4825–4841, <https://doi.org/10.1002/2015JD023178>.
- 920 Wang, J., H. Luo, Q. Yang, J. Liu, L. Yu, Q. Shi, and B. Han, 2022a: An Unprecedented Record  
921 Low Antarctic Sea-ice Extent during Austral Summer 2022. *Advances in Atmospheric*  
922 *Sciences*, **39**, 1591–1597, <https://doi.org/10.1007/s00376-022-2087-1>.

- 923 Wang, S., M. Ding, G. Liu, and W. Chen, 2022b: Processes and Mechanisms of Persistent  
924 Extreme Rainfall Events in the Antarctic Peninsula during Austral Summer. *Journal of*  
925 *Climate*, **35**, 3643–3657, <https://doi.org/10.1175/JCLI-D-21-0834.1>.
- 926 Wille, J. D., V. Favier, A. Dufour, I. V. Gorodetskaya, J. Turner, C. Agosta, and F. Codron,  
927 2019: West Antarctic surface melt triggered by atmospheric rivers. *Nature Geoscience*,  
928 **12**, 911–916, <https://doi.org/10.1038/s41561-019-0460-1>.
- 929 —, and Coauthors, 2021: Antarctic Atmospheric River Climatology and Precipitation Impacts.  
930 *Journal of Geophysical Research: Atmospheres*, **126**, e2020JD033788,  
931 <https://doi.org/10.1029/2020JD033788>.
- 932 —, and Coauthors, 2022: Intense atmospheric rivers can weaken ice shelf stability at the  
933 Antarctic Peninsula. *Communications Earth and Environment*, **3**, 1–14,  
934 <https://doi.org/10.1038/s43247-022-00422-9>.
- 935 WMO (ed.), 1992: International Meteorological Vocabulary. WMO No. 182, World  
936 Meteorological Organization, Geneva, Switzerland, 784 pp.
- 937 Xu, M., L. Yu, K. Liang, T. Vihma, D. Bozkurt, X. Hu, and Q. Yang, 2021: Dominant role of  
938 vertical air flows in the unprecedented warming on the Antarctic Peninsula in February  
939 2020. *Communications Earth and Environment*, **2**, 1–9, [https://doi.org/10.1038/s43247-](https://doi.org/10.1038/s43247-021-00203-w)  
940 [021-00203-w](https://doi.org/10.1038/s43247-021-00203-w).
- 941 Zou, X., D. H. Bromwich, A. Montenegro, S.-H. Wang, and L. Bai, 2021a: Major surface  
942 melting over the Ross Ice Shelf part I: Foehn effect. *Quarterly Journal of the Royal*  
943 *Meteorological Society*, **147**, 2874–2894, <https://doi.org/10.1002/qj.4104>.

- 944 ———, ———, ———, ———, and ———, 2021b: Major surface melting over the Ross Ice Shelf part II:  
945 Surface energy balance. *Quarterly Journal of the Royal Meteorological Society*, **147**,  
946 2895–2916, <https://doi.org/10.1002/qj.4105>.
- 947 Zhang, Z., Ralph, F.M., Zou, X., Kawzenuk B., & Gorodetskaya I., 2023: Atmospheric River  
948 Scale for the Polar Regions. *Journal of Geophysical Research: Atmospheres*. In  
949 preparation.